*Marked Revision
Click here to download Marked Revision: Al Electrochem_Revision_Changes shown 01Mar13.docx
Click here to view linked References

Electrochemical Behaviour of Aluminium in Electrocoagulation Processes

Martin Mechelhoff[a,1], Geoff H. Kelsall[a], Nigel J.D. Graham[b*]

[a] Department of Chemical Engineering, Imperial College London, London SW7 2AZ, United Kingdom (g.kelsall@imperial.ac.uk)

&

[b] Department of Civil and Environmental Engineering, Imperial College London, London SW7 2AZ, United Kingdom (n.graham@imperial.ac.uk)

[1] Present address: Lanxess Deutschland GmbH, Group Function Innovation & Technology, 51369 Leverkusen, Germany (martin.mechelhoff@lanxess.com)

*Corresponding author: Tel: +44 207 5946121; Fax: +44 207 5945934; n.graham@imperial.ac.uk (N.J.D. Graham)

Abstract

Passivation of aluminium electrodes is a common problem in electrocoagulation reactors used for the purification of natural waters, leading to high cell voltages and compromising the viability of such industrial processes. In order to identify possible mitigation strategies, cyclic voltammetric, potentiostatic and galvanostatic measurements were made to investigate the effects of electrode surface topography and solution composition on the electrochemical behaviour of pure aluminium and Al 1050 in neutral electrolyte solutions. In addition, electrochemical impedance spectroscopy was used to estimate thicknesses of passive layers before and after dissolution. Chloride ions, well-known pitting promoters, were found to facilitate dissolution of passive surfaces, though attenuated by the presence of the naturally-occurring contaminant humic acid. Under galvanostatic conditions, a smooth aluminium electrode showed a constant rise in electrode potential due to passivation. However, even in the absence of pitting promoters electrodes with a 'rough' surface finish (R_a-values > 1 μm) exhibited an initial potential increase, followed by a dramatic decrease to relatively low steady state values due to 'spontaneous de-passivation'. The precipitation of dissolved aluminium(III), releasing H^+ ions, was identified as the probable cause of this effect, leading to acidic pH values, locally dissolving the passive layer and enhancing dissolution rates.

Keywords: electrochemistry; coagulation, chemical processes; separations; aluminium dissolution, passivation.

46 **Notation**

Symbol	Meaning	Units
A_e	Electrode area	m^2
c	Concentration	mol m^{-3}
C	Area specific capacitance	F m^{-2}
d	Passive layer thickness	m
D	Diffusion coefficient	m^2 s^{-1}
E	Electrode potential vs. reference electrode	V
E_{eqm}	Equilibrium potential vs. reference electrode	V
F	Faraday constant, 96 485	C mol^{-1}
$\vec{F}$	Volume force field	N m^{-3}
j	current density	A m^{-2}
j_0	Exchange current density	A m^{-2}
K	Equilibrium constant	
k_i	Standard rate coefficient for reaction i	m s^{-1}
n	Exponent in equation (37); $n = 1/(D\text{-}1)$, where D is the fractal dimension	1
p	Pressure	Pa
R	Gas constant, 8.314 472	J mol^{-1} K^{-1}
R	Reaction rate	mol m^{-3} s^{-1}
R_a	Degree of surface roughness	µm
SHE	Standard hydrogen electrode	-
t	Time	s
T	Temperature	K
$u_{m,i}$	Ionic mobility (equation 42)	m^2 mol J^{-1} s^{-1}
$\vec{u}$	Velocity	m s^{-1}
Y_0	Area specific admittance (equation 37)	F s^{1-n} m^{-2}

z	Electron stoichiometric factor / reaction charge number	1
Z’	Impedance, real part	$\Omega\ m^2$
Z’’	Impedance, imaginary part	$\Omega\ m^2$
$\Delta_f G_i^{\ominus}$	Gibbs energy of formation of species *i*	$J\ mol^{-1}$
$\Delta_r G^{\ominus}$	Gibbs energy of formation of reaction	$J\ mol^{-1}$
ε	Permittivity	$F\ m^{-1}$
ε_r	Relative permittivity	1
ϕ	Potential	V
η	Overpotential, (E - E_{eqm}) (equation 40)	V
η	Dynamic viscosity (equation 41)	Pa s
ν	Stoichiometric number	1
ν_e	Electron stoichiometric number of reaction	1
ρ	Density of electrolyte solution	$g\ m^{-3}$
ρ_{Al}	density of aluminium	$g\ m^{-3}$
ω	Angular frequency	$rad\ s^{-1}$

47

1. Introduction

Electrocoagulation is a water purification process that uses electrical energy to dissolve metals, such as aluminium and iron, to destabilise colloidal suspensions resulting in the flocculation of contaminants. It obviates the need for additions of aqueous solutions of Al^{III} or Fe^{III} coagulants, required by conventional chemical coagulation methods, as used for purifying potable water.

The feasibility of applying electrocoagulation in the purification of a great variety of raw waters has been reported widely, e.g. for removal of dissolved arsenic from ground water and wastewater (Kumar, 2004; Parga et al., 2005), but comparatively few reports have analysed the process in detail (e.g. Chen et al., 2002). Increased efficiencies of a continuous reactor have been achieved by additional injection of air bubbles into the inlet stream, so that increased inter-particle contact led to a higher flocculation rate (Parga et al., 2005). Both aluminium and iron electrodes have been used to remove up to 64% of the initial chemical oxygen demand in effluents from textile manufacture (Kobya, 2003; Can, 2006). Continuous electrocoagulation reactors with aluminium electrodes have also been used to separate mineral oil from wastewater (Khemis, 2005; Carmona et al., 2006) and, using a laboratory batch reactor, to remove clay particles from aqueous dispersions (Holt et al., 2004).

A continuous single pass electrocoagulation reactor with parallel plate electrodes was used to produce potable water by removal of 96 % of colour and 71 % of total organic carbon (TOC) from a Norwegian surface water, using a dosage of 6 g m^{-3} aluminium(III) (Vik et al., 1984). Synthetic solutions representing natural upland water were purified of humic acid, a source of organic carbon and colour, using a laboratory electrocoagulation reactor (Jiang et al., 2002). An aluminium(III) concentration of 3.6 g m^{-3} resulted in removal of 60 % of TOC and ca. 90 % of colour, as opposed to 30

and 60 %, respectively, when conventional coagulation methods were used with the same dosage.

However, very few publications describe the electrochemical processes occurring during electrocoagulation. One such paper (Mouedhen et al., 2008) reported aluminium anode potentials of 35 V (SCE) in sodium sulphate solution, but which decreased substantially with increasing concentrations of NaCl; no explanation for this behaviour was offered, although chloride-induced de-passivation must have been responsible.

Evidently, further development and optimisation of electrocoagulation reactors can be achieved only with adequate knowledge of the electrochemical reactions and the effects of solution composition and surface chemistry, as well as topography, on aluminium dissolution rates.

A study (Heusler and Allgaier, 1971) of the oxidative dissolution kinetics of high purity aluminium electrodes in 500 mol m^{-3} sodium sulphate solutions with pH values of 9.5 to 14, enabled the derivation of pH dependent values of diffusion coefficients for dissolved aluminium(III) species. The corrosion and passivation behaviour has also been reported for high purity aluminium in solutions containing acetic acid and sodium acetate with pH values between 3.7 and 6.7 (Hurlen et al., 1984) and in 1000 mol m^{-3} NH_4Ac to which various concentrations of ammonia were added to achieve pH values between 7.2 and 9.9 (Hurlen and Haug, 1984). Tafel slopes for aluminium dissolution were found to depend on solution pH, and a relationship was developed of the potential dependence of the oxide layer thickness on aluminium electrodes for these specific experimental conditions (Hurlen et al., 1984). The kinetics of aluminium dissolution in 100 to 4000 mol m^{-3} KOH have also been reported (Brown and Whitley, 1987; Diggle and Ashok, 1976).

Recently, an extensive model (Guseva et al., 2009) of the dissolution process at a single corrosion pit on an aluminium surface in sodium chloride containing aqueous solutions predicted that hydrolysis of aluminium(III) leading to $Al(OH)^{2+}$ and releasing H^{+} ions was responsible for local pH values < 3 at the bottom of the pit.

However, there is still a paucity of information about aluminium dissolution kinetics in neutral solutions of inert electrolytes, such as sodium sulphate, due to the difficulties arising from the formation of passive oxide and hydroxide for electrochemical measurements at these pH values. In addition, little is known about the effects on the dissolution process of complex organic compounds like humic acid, representing natural organic matter as one of the main contaminants in natural water.

Hence, the aims of the work for which results are reported below were to understand how dissolution of aluminium could occur in waters of pHs at which it is known to form passive oxide layers and to devise strategies for obviating such problems, enabling improved electrocoagulation process performance in purifying water from natural sources. The objectives were: i) to determine the effects of surface pre-treatment and solution composition on aluminium oxidation and dissolution kinetics in neutral aqueous electrolyte solutions; ii) to estimate the effective thicknesses of oxide layers from electrochemical impedance spectroscopic measurements as functions of electrode potential and applied current density. An accompanying second paper by the authors aims to explain why aluminium was found to exhibit apparent super-faradaic charge yields for its dissolution as aluminium(III), as had been reported in the literature. The apparent electron stoichiometry is required for prediction of dosing concentrations from applied currents in electrocoagulation processes.

In an electrochemical system representing an electrocoagulation reactor, the anode consists of aluminium (in our case), whereas the cathode may be made of an inert

material, such as platinised titanium or stainless steel. The aluminium anode is dissolved electrochemically, but at electrode potentials $E < E_{H_2O/H_2}$, hydrogen evolution may occur in parallel:

$j_{a,Al}$ $$Al \rightarrow Al^{III} + 3e^- \quad (1)$$

j_{c,H_2} $$2H_2O + 2e^- \rightarrow H_2 + 2OH^- \quad (2)$$

Hence, the net current is: $$j_{net} = j_{a,Al} + j_{Al,H_2} \quad (3)$$

At the inert cathode, hydrogen evolution by reaction (2) was considered the sole reaction at a current density j_{c,H_2}.

Due to the low solubility of Al^{III} species at neutral pH, $Al(OH)_3$ was considered to precipitate homogeneously in the bulk solution by a two-step process:

$$Al^{3+} + H_2O \underset{k_{-1}}{\overset{k_1}{\rightleftharpoons}} Al(OH)^{2+} + H^+ \quad (4)$$

$$Al(OH)^{2+} + 2H_2O \underset{k_{-2}}{\overset{k_2}{\rightleftharpoons}} Al(OH)_3 + 2H^+ \quad (5)$$

Since the solution was de-oxygenated by bubbling nitrogen (see section 3), no current for the reduction of oxygen at the anode and cathode needed to be considered.

2. Thermodynamics of Al-H_2O Systems

The superimposed potential-pH diagrams for the stable and meta-stable aluminium-water systems (Figure 1) predict Al_2O_3 and / or (meta-stable) $Al(OH)_3$ to form in solutions of neutral pH at potentials > -2.2 V (SCE). The aqueous chemistry is more complex than implied by the list of species in (Perrault, 1985), as there is convincing evidence for polymeric species, the best characterised (Bottero et al., 1980; Billik and Horváth, 2008; Lin and Lee, 2010) of which is $\left[Al_{13}O_4 \left(OH \right)_{24} \right]^{7+}$. Its Gibbs energy of

formation ($\Delta_f G^{\theta}$) of -12 372 908 J mol^{-1} was calculated from the equilibrium constant (K) (Baes and Mesmer, 1976) for the reaction:

$$13Al^{3+} + 28H_2O \rightleftarrows \left[Al_{13}O_4(OH)_{24}\right]^{7+} + 32H^+ \quad ; \quad \log K = -100.4 \qquad (6)$$

These data were added to those listed in Perrault (1985) and used to calculate Figure 1, Figure 2 and Figure 3 with a spreadsheet. For the general reaction:

$$pA_q + rH^+ + \nu_e e^- \rightleftarrows qB_p + cH_2O \qquad (7)$$

$$\Delta_r G^{\theta} = \sum_i \nu_{p,i} \Delta_f G^{\theta}(\text{products}) - \sum_j \nu_{r,j} \Delta_f G^{\theta}(\text{reactants}) = -\nu_e F E^{\theta} \qquad (8)$$

Hence,

$$E_{B/A}\,(\text{SHE})/\,\text{V} = E^{\theta}_{B/A} - \frac{0.0591 \cdot r}{\nu_e} pH + \frac{0.0591}{\nu_e} \log\left\{c_T^{\,(p-q)} q^{-p} p^q\right\} \qquad (9)$$

Whereas for a chemical reaction ($\nu_e = 0$):

$$\Delta_r G^{\theta} = \sum_i \nu_{p,i} \Delta_f G^{\theta}(\text{products}) - \sum_j \nu_{r,j} \Delta_f G^{\theta}(\text{reactants}) = -\ln(10) RT \log_{10} K \qquad (10)$$

For the metastable system in equilibrium with amorphous $Al(OH)_3$, $\left[Al_{13}O_4(OH)_{24}\right]^{7+}$ species were predicted to predominate at pH < 5.5, as shown in Figure 2b:

$$13Al(OH)_3(am) + 7H^+ \rightleftarrows \left[Al_{13}O_4(OH)_{24}\right]^{7+} + 11H_2O \qquad (11)$$

$$\log\left(\left[Al_{13}O_4(OH)_{24}\right]^{7+}\right) = 33.82 - 7\,pH \qquad (12)$$

Hence, the Nernst equation for the meta-stable system is plotted in Figure 1 in the restricted pH range ca. 4.7 – 5.4 for a dissolved Al^{III} activity of 10^{-4}, for the reaction:

$$\left[Al_{13}O_4(OH)_{24}\right]^{7+} + 32H^+ + 39e^- \rightleftarrows 13Al + 28H_2O \qquad (13)$$

160 $$E\left(\mathrm{SCE}\right) / \mathrm{V} = -1.7683 - 0.0485\,pH + 0.0015\log\left(\left[Al_{13}O_4\left(OH\right)_{24}\right]^{7+}\right) \quad (14)$$

161 To produce a bulk concentration (assuming concentration ≈ activity) of dissolved
162 aluminium(III) of 10^{-4} mol dm^{-3} typical of electrocoagulation processes operating with a
163 neutral feed solution, Figure 2a predicts that pH values < 4.7 are needed for Al^{3+} ions to
164 be dissolved from Al_2O_3, whereas Figure 2b predicts that pH values need to be
165 decreased to < 5.4 to dissolve $\left[Al_{13}O_4\left(OH\right)_{24}\right]^{7+}$ ions from amorphous $Al(OH)_3$.

166 As suggested by Dražić and Popić (1993), aluminium may dissolve by reactions with
167 electron stoichiometries potentially < 3; hence, greater concentrations of dissolved
168 aluminium than implied by equation (1) would result at any current density. Results of
169 aluminium electrode potential measurements as a function of pH and dissolved
170 aluminium concentration caused Perrault to postulate the formation of dissolved
171 aluminium hydride species, such as AlH^{2+} ions, in addition to the solid AlH_3 phase
172 (Perrault, 1979). Corrosion due to hydrogen evolution was excluded by weight loss
173 measurements before and after experiments, but the precision was not specified. Only
174 the metastable $Al(OH)_3$ phase, rather than the more stable Al_2O_3 phase was included in
175 the calculations; the relative stabilities of the two phases is evident from Figure 2.

176 The potential-pH diagram(s) in Figure 3 was calculated using Gibbs energies of
177 formation, critically assessed by Perrault (1985), for aluminium species and phases. The
178 diagram considering Al / Al_2O_3 phases predicted the expected solubility as Al^{3+} ions at
179 low pH and as $Al(OH)_4^-$ ions at high pH, as in Figure 1 and Figure 2a. When AlH^{2+} ions
180 and AlH_3 were included in the calculations, AlH_3 predominated over Al at low
181 potentials, with a polygonal area of stability of AlH^{2+} ions at less negative potentials
182 and pH less than about 11. At even less negative potentials, Al^{3+} ions were predicted to
183 form, with Al_2O_3 then $Al(OH)_4^-$ ions predominating with increasing pH, as in Figure 2a.

184 The Nernst equation (16) for the reaction:

185 $$Al + 3H^+ + 3e^- \longrightarrow\!\!\!\!\!\!\leftarrow AlH_3\,(electrochem.) \qquad (15)$$

186 $$E_{Al/AlH_3}\,(\mathrm{SCE})\ /\ \mathrm{V} = -0.604 - 0.0592\,pH \qquad (16)$$

187 confirms the lack of stability of Al for any potential-pH conditions, as Al^{3+} ions | Al_2O_3 |
188 $Al(OH)_4^-$ ions rather than Al would be stable at potentials predicted by Figure 1, since
189 the Nernst equation (18) for the reaction:

190 $$Al^{3+} + 3H^+ + 6e^- \longrightarrow\!\!\!\!\!\!\leftarrow AlH_3\,(electrochem.) \qquad (17)$$

191 $$E_{Al^{3+}/AlH_3}\,(\mathrm{SCE})\ /\ \mathrm{V} = -1.262 - 0.0296\,pH + 0.010\log\left(Al^{3+}\right) \qquad (18)$$

192 corresponds to potentials more negative than those of equation (16).

193 As shown in Figure 3, the oxidation of AlH_3 is predicted to occur at potentials greater
194 than those given by the Nernst equation (20) for the reaction:

195 $$AlH^{2+} + 2H^+ + 4e^- \longrightarrow\!\!\!\!\!\!\leftarrow AlH_3\,(electrochem.) \qquad (19)$$

196 $$E_{AlH^{2+}/AlH_3}\,(\mathrm{SCE})\ /\ \mathrm{V}\ = -1.461 - 0.0296\,pH + 0.0148\log\left(AlH^{2+}\right) \qquad (20)$$

197 Or at pH values > ca. 11, by the reaction:

198 $$Al\left(OH\right)_4^- + 7H^+ + 6e^- \longrightarrow\!\!\!\!\!\!\leftarrow AlH_3 + 4H_2O \qquad (21)$$

199 $$E_{Al(OH)_4^-/AlH_3}\,(\mathrm{SCE})\ /\ \mathrm{V}\ = -1.027 - 0.069\,pH + 0.0099\log\left(Al\left(OH\right)_4^-\right) \qquad (22)$$

200 The upper bounds of the polygon defining the stability range of AlH^{2+} ions are defined
201 by the reactions (23), (25) and (27), with corresponding Nernst equations (24), (26) and
202 (28):

203 $$Al^{3+} + H^{+} + 2e^{-} \rightleftarrows AlH^{2+} \quad (23)$$

204 $$E_{Al^{3+}/AlH^{2+}}\left(\mathrm{SCE}\right) / \mathrm{V} = -0.864 - 0.0296\,pH + 0.0296 \log\left\{\left(Al^{3+}\right)/\left(AlH^{2+}\right)\right\} \quad (24)$$

205 $$Al_2O_3 + 8H^{+} + 4e^{-} \rightleftarrows 2AlH^{2+} + 3H_2O \quad (25)$$

206 $$E_{Al_2O_3/AlH^{2+}}\left(\mathrm{SCE}\right) / \mathrm{V} = -0.607 - 0.1183\,pH - 0.0148 \log\left(AlH^{2+}\right) \quad (26)$$

207 $$Al\left(OH\right)_4^{-} + 5H^{+} + 2e^{-} \rightleftarrows AlH^{2+} + 4H_2O \quad (27)$$

208 $$E_{Al(OH)_4^{-}/AlH^{2+}}\left(\mathrm{SCE}\right) / \mathrm{V} = -0.159 - 0.1479\,pH - 0.0296 \log\left(AlH^{2+}\right) \quad (28)$$

209 Were Figure 3 for the metastable system to be used to predict the kinetic behaviour of
210 Al anodes, then active dissolution would be expected over the potential-pH range of
211 predicted stability of AlH^{2+} ions, even if net current densities were negative due to
212 concurrent hydrogen evolution at such potentials. Results of dissolution experiments
213 reported previously (Holt et al., 2004; Vik et al., 1984; Jiang et al., 2002) provided no
214 evidence of such behaviour or support for the hypothesis of the existence of AlH^{2+} ions;
215 reversal of the sign of the net currents occurred at ca. -1.45 V (SCE) and potential-
216 independent current densities of ca. 0.1 A m^{-2} occurred at potentials > -1.3 V (SCE),
217 presumably due to passivation by oxide film formation.

218 While the thermodynamic properties (Qiu et al, 2004) and kinetic behaviour of AlH_3 are
219 well-established, it has been reported (Adhikari and Hebert, 2008; Adhikari et al, 2010)
220 to form at low potentials primarily at high pH > 11, as may result locally when
221 hydrogen evolution occurs on aluminium in neutral aqueous solutions. In addition to
222 reactions (17) and (21), reactions (29) and / or (31) and their respective Nernst

equations (30) and (32) define the upper potential boundary with Al^{III} species and phases.

$$Al_2O_3 + 12H^+ + 12e^- \rightleftharpoons 2AlH_3\left(electrochem.\right) + 3H_2O \quad (29)$$

$$E_{Al_2O_3/AlH_3}\left(\mathrm{SCE}\right) / \mathrm{V} = -1.176 - 0.0592\,pH \quad (30)$$

$$Al\left(OH\right)_3 + 6H^+ + 6e^- \rightleftharpoons AlH_3\left(electrochem.\right) + 3H_2O \quad (31)$$

$$E_{Al(OH)_3/AlH_3}\left(\mathrm{SCE}\right) / \mathrm{V} = -1.190 - 0.0592\,pH \quad (32)$$

The issue of effective electron stoichiometry for aluminium oxide will be addressed further in the accompanying paper.

3. Experimental

An Ecochemie Autolab PGStat30 was used, which included a frequency response analysis (FRA) module, for electrochemical impedance spectroscopy. All chemicals (Na_2SO_4, NaCl and humic acid) were of reagent grade (Sigma-Aldrich). High purity water for the experiments was produced by reverse osmosis (Elga Elgastat Prima) and de-ionisation (Elga Elgastat Maxima) to give a conductivity of 1.0×10^{-6} S m^{-1}. Fresh solutions were prepared for all measurements, and were deoxygenated with high purity N_2 gas for 30 minutes prior to the start of an experiment, and kept under an N_2 atmosphere throughout, to prevent the ingress of atmospheric oxygen; the residual dissolved oxygen concentration was below the detection limit of a Hach-Lange dissolved oxygen electrode. No pH adjustment was carried out, so that the pH of the bulk solution was ca. 7. Due to its mildly acidic properties, a solution containing 10 g m^{-3} of humic acid had a pH of ca. 6.5.

A three compartment glass cell was used, with a saturated calomel reference electrode (Cole-Parmer) in a Luggin probe and a ca. 100 mm^2 platinum flag counter electrode (Goodfellow Ltd., UK) separated from the main compartment by a porous glass frit to prevent hydrogen bubbles from disturbing measurements.

3.1. Cyclic voltammetry

Voltammetric measurements were carried out with a rotating disc system (Pine Instruments Inc.) capable of rotation rates of 60 – 2000 rpm. An aluminium disc of 99.99% purity with a diameter of 5 mm formed the working electrode. Prior to each measurement it was polished wet with 50 nm alumina powder (Sigma-Aldrich) to achieve a mirror finish. After being immersed in the electrolyte solution, a potential of -2.3 V (SCE) was applied for 4 minutes to evolve hydrogen by reaction (2), thereby dissolving / thinning the air-formed oxide layer on the working electrode, to achieve reproducible surfaces from which to start experiments, such that subsequent behaviour was independent of electrode history.

Electrolyte solutions contained 0.5 mol m^{-3} Na_2SO_4 with the addition of 0.4 mol m^{-3} NaCl and 5 to 10 g m^{-3} humic acid, where necessary. These solutions represented the main components of the natural raw water at a typical water treatment works in West Yorkshire (UK) with typical contaminant concentrations and conductivity.

3.2. Electrochemical impedance spectroscopy

To estimate the dependence of the passive layer thickness on the applied electrode potential, impedance spectra were measured in solutions of 0.5 mol m^{-3} Na_2SO_4 with addition of 10 g m^{-3} humic acid and 0.15 mol m^{-3} NaCl at potentials typical for aluminium dissolution: -1.0, -0.6, and -0.2 V (SCE); due to the occurrence of time-dependent currents caused by pitting, -0.4 V (SCE) was applied as the final potential for

the chloride containing solution. Measurements were made in a frequency range of 10^4 to 10^{-3} Hz and with an amplitude of 10 mV (p-p) (Jüttner and Lorenz, 1989; Martin et al., 2005). Only data generated at frequencies greater than 0.1 Hz were subject to fitting of an equivalent analogue circuit and are presented here, since impedances at lower frequencies did not show a dependence on applied potential and therefore were considered of no use for data analysis.

A three compartment glass electrode cell was used with a working electrode consisting of a vertical rectangular aluminium plate Al1050 (99.5 % purity) of area 3.57×10^{-5} m^2 connected to a copper wire that was shrouded by a glass tube and sealed with epoxy resin at both ends, resulting in a co-planar surface with the electrode surface. Prior to each measurement, the electrode was polished to mirror finish with 50 nm alumina powder (Sigma-Aldrich), then rinsed with high purity water, immersed in 10 mol m^{-3} NaOH for 4 minutes, and then immersed into the measurement solution. Its potential was controlled at -2.3 V (SCE) for 5 minutes and at the measurement potential for 30 minutes before an impedance measurement was started.

3.3. Galvanostatic measurements

Two types of electrode materials were used: pure aluminium (99.99 % purity; Alfa-Aesar) and technical grade aluminium 1050 (99.5 %; Aldruscilla, London). In order to avoid contamination of the produced water with alloying elements, specifically pure electrode material has to be used in electrocoagulation reactors. Aluminium 1050 was the purest aluminium alloy commercially available in an industrial scale. Table 1 lists the maximum concentrations of the main impurities in Al 1050, as given by the manufacturer.

(Table 1 here)

In order to provide surface conditions that were more realistic for industrial processes, the pre-treatment procedure of the working electrode was simplified compared to the impedance measurements (section 3.2). The electrodes were prepared in two ways:

a) rough electrodes: dry polished with P1200 SiC paper (Buehler), then rinsed with high purity water.

b) smooth electrodes: dry polished with P1200 SiC paper (Buehler), then wet polished with 300 and with 50 nm alumina, finally rinsed with high purity water.

The roughness of the electrodes was measured with a Zygo white light interferometer. Table 2 lists typical roughness values for each electrode, together with the geometrical electrode area and applied current density.

(Table 2 here)

A current of 1×10^{-4} A ($\equiv$ ca. 3 A m^{-2}) was applied for 10 minutes during each experiment and the electrode potential recorded as a function of time. An impedance spectrum was measured at a potential of -0.55 V (SCE) in a frequency range of 1×10^{-4} Hz to 5×10^{-2} Hz before and after the current was applied. Prior to an impedance measurement, a constant potential of -0.55 V (SCE) was applied for 30 minutes to ensure a time-independent current signal. This potential was chosen to be above the reversible potential for hydrogen evolution $E_{H_2O/H_2} = -0.65$ V (SCE) at pH 7 and below the pitting potential $E_{pit} = -0.52$ V (SCE). Hydrogen evolution can complicate the measurement by providing a non-representative net current, whereas pitting is responsible for a time-dependent current that needs to be avoided if meaningful impedance measurements are to be obtained.

4. Results and Discussion

4.1. Voltammetry at Al rotating disc electrodes

In an attempt to achieve reproducible aluminium electrode surfaces from which to start experiments, a potential of -2.3 V (SCE) was applied for 4 minutes to evolve hydrogen by reaction (2) after the electrode had been immersed in the electrolyte solution. Reproducible surfaces were achieved by dissolving / thinning the air-formed oxide layer on the working electrode. Figure 1 predicts aluminium is stable at this potential, whereas Figure 3 predicts that the hydride phase, AlH_3, should form. Air-formed oxide and hydroxide films due to aluminium reacting with water and oxygen (Diggle and Ashok, 1976) can be dissolved chemically ('cathodically') (Azumi et al., 2004; Takahashi et al., 1994; Ogle et al., 2011) by hydroxide ions produced by reaction (2) occurring at the defects in the oxide layer at the base of pores:

$$2H_2O + 2e^-_{(Al)} \xrightarrow{k_c} H_2 + 2OH^-_{(x=0)} \quad \downarrow k_m \quad 2OH^-_{(x=\delta)} \qquad (2)$$

coupled to:

$$Al(OH)_3(am) + OH^- \longrightarrow Al(OH)_4^- \qquad (33)$$

and / or:

$$Al_2O_3(c) + 3H_2O + 2OH^- \longrightarrow 2Al(OH)_4^- \qquad (34)$$

Depending on the applied potential, the underlying aluminium may also be oxidised, forming pits. In addition, AlH_3 (Adhikari and Hebert, 2008; Lin et al., 1994; Adhikari et al., 2008; Adhikari et al., 2010; Perrault, 1979) may have formed by e.g. reaction (15), as discussed in our accompanying paper.

Restricted rates of diffusional and migrational transport of hydroxide ions away from the base of pores with rate coefficient k_m (reaction (2)) would have caused the local pH to become alkaline, thereby dissolving (hydr-)oxide by reactions (33) and (34). Hence,

in a subsequent potential scan to positive potentials, the experimental trajectory in potential-pH space would have been diagonal (Figure 1 or Figure 3) as the local pH relaxed towards its bulk value in the unbuffered solution with decreasing rate of reaction (2).

Figure 4 shows a Tafel plot for a linear potential sweep between -2.3 and 0.5 V (SCE) at a rotating disc electrode; Tafel-type behaviour was evident for potentials < -1.9 V (SCE), at which hydrogen evolution was predicted by Figure 1 to be the sole reaction, with AlH_3 formation predicted by Figure 3. The potential of the reversal of the net current from negative to positive can be estimated from Figure 4 as -1.45 V (SCE), corresponding to -1.70 V (SHE); this value is more positive than the equilibrium potentials for the formation of $Al(OH)_3$ and Al_2O_3, respectively, as determined by their respective Nernst equations:

$$E_{Al(OH)_3/Al}\ (\text{SCE})\ /\ \text{V} = -1.717 - 0.0592 \cdot pH \qquad (35)$$

$$E_{Al_2O_3/Al}\ (\text{SCE})\ /\ \text{V} = -1.749 - 0.0592 \cdot pH \qquad (36)$$

Hence, at pH 7, $E_{Al(OH)_3/Al} = -2.131$ V (SCE) and $E_{Al_2O_3/Al} = -2.163$ V (SCE), whereas the reversible potential for the evolution of hydrogen is ca. -0.65 V (SCE) at pH of 7. Therefore, at potentials between -2.1 and -0.65 V (SCE), measured current densities j_{net} (equation (3)) were composed of partial current densities for aluminium oxidation j_{Al} and for water reduction j_{H_2} by reaction (2). Hence, the absolute magnitude of j_{net} would have been smaller than each of its partial current densities j_{Al} and j_{H_2}, which would have been of equal magnitude at the potential corresponding to zero net current.

For potentials more positive than the reversible potentials given by equations (35) and (36), passivation resulted from the formation of Al_2O_3 / $Al(OH)_3$, across which most of

359 the potential was dropped, resulting in current densities being independent of the
360 applied potential for values more positive than -1.3 V (SCE), as evident in Figure 4.

361 Humic acid and chloride ions are the main components of natural water that may affect
362 the electrochemical behaviour of aluminium electrodes. Figure 5 shows typical cyclic
363 voltammograms of an aluminium electrode in solutions containing sodium sulphate,
364 sodium chloride and humic acid, compared to the behaviour in a solution of sodium
365 sulphate alone. On a positive-going potential scan from -2.1 V (SCE), hydrogen
366 evolution was the predominant reaction until its reversible potential of -0.65 V (SCE),
367 above which in pure sodium sulphate solution, current densities were very small due to
368 passivation (Figure 5 d).

369 The addition of chloride ions to the sodium sulphate solution (Figure 5 a)) led to a
370 dramatic increase in dissolution current densities for potentials > -0.52 V (SCE), due to
371 pitting (Szklarska-Smialowska, 1986), for which chloride ions are well-known
372 promoters. The initially increased current density on the negative-going potential sweep
373 back from 0.0 to -2.1 V (SCE) was due to the larger surface area created by the pits. The
374 measured pitting potential E_{pit} of -0.52 V (SCE), was close to the value of -0.49 V
375 (SCE) reported for similar conditions (Lee, 2000). When humic acid of concentrations 5
376 and 10 mg dm^{-3} was added to the chloride-containing solution, the increased current
377 densities for potentials more positive than E_{pit} were much less pronounced (Figure 5,
378 graphs b) and c)). A higher humic acid concentration resulted in decreasing oxidation
379 current densities, though the basic behaviour and value of E_{pit} remained unchanged.
380 Humic acids contain aromatic nuclei with carboxylic and phenolic substituents, so
381 behave as mixtures of dibasic acids, with $pK_{a1} \approx 4$ for protonation of carboxylate groups
382 and $pK_{a2} \approx 8$ for protonation of phenolate groups. Hence, anionic carboxylate groups
383 would predominate at neutral pHs, so could adsorb electrostatically on positively

charged aluminium oxide surfaces (p.z.c. at pH 9.1), and / or by chemisorption or chemical reaction. Hydroxy carboxylic acids (Bereket and Yurt, 2001) and sodium decanoate (Boisier et al., 2010) also have been reported to act as corrosion and pitting inhibitors for aluminium alloys.

Hence, sodium chloride is an essential for efficient dissolution of aluminium in neutral aqueous solutions, since it triggers the growth of pits that lead to dramatically increased dissolution current densities at electrode potentials greater than E_{pit}. The presence of humic acid in the solution diminishes this effect; however, complete passivation of the electrode surface caused by the adsorption of humic acid was not observed in the concentration range studied.

4.2. Effect of Electrode Potential on Passive Layer Thickness

Electrochemical impedance spectroscopy was used to determine the potential dependence of the capacitance and hence the thickness of the passive oxide/hydroxide layer, together with the effects of the solution components sodium sulphate, sodium chloride and humic acid thereon.

Figure 6 shows impedance spectra for a stationary aluminium 1050 electrode at frequencies of ca. 10^{-2} – 10^{4} Hz for electrode potentials of -1.0, -0.6 and -0.2 V (SCE) in solutions containing sodium sulphate, humic acid and sodium chloride. For all potentials and in all solutions, a semi-circle was observed that overlapped with another semi-circle at lower frequencies. The radius of the semi-circles and hence the maximum imaginary impedance $-Z''_{max}$, appeared at frequencies of about 1 Hz for all measurements, and clearly increased with increasingly positive electrode potentials. In pure sulphate solution, $-Z''_{max}$ reached values in the range 0.3 to 1.5 $\Omega\,m^2$, whereas addition of humic acid and sodium chloride resulted in lower values of ca. 0.35 $\Omega\,m^2$ to 1.2 $\Omega\,m^2$ and ca. 0.2 to 0.7 $\Omega\,m^2$, respectively.

These results agree with previously published (Martin et al., 2005) impedance data for aluminium in 0.01 mol dm^{-3} NaCl, for which a slightly depressed semi-circle was found to grow in diameter with increasing applied potential, ascribed to a growing passive layer thickness.

The magnitude of the maximum imaginary impedance $-Z''_{max}$ was clearly dependent on the electrode potential, showing a linear increase with more positive potential. At a potential of -1.0 V, the values of $-Z''_{max}$ were similar in all solutions; however, when humic acid and sodium chloride were added, the gradient of the straight line decreased considerably, with the chloride containing solution resulting in the smallest gradient (Figure 7). Therefore, the interfacial electrical properties of the passive layer changed, due to both humic acid and chloride ions adsorbing on the electrode surface.

The impedance data measured in pure sodium sulphate solution were fitted with a 'complex non-linear least squares' (CNLS) procedure using a program provided in the Autolab software, based on Boukamp's method (Boukamp, 2004). Having tried several possible equivalent circuits, e.g. that proposed by Jüttner and Lorenz (1989), the circuit suggested by Martin et al. (2005) proved most suitable (Figure 8). Here, CPE1 and R1 refer to the porous top structure of the passive oxide layer, whereas R2 and CPE2 represent the properties of the underlying dense barrier layer. Pébère and Boisier (2008) suggested an identical circuit to model a porous aluminium oxide layer on aluminium AA2024 that developed during anodising in acidic solutions. However, Hitzig et al. (1984) used a slightly different circuit for a porous aluminium oxide layer, where the partial circuit R_2-CPE_2 from the model above was removed and R_e replaced with a capacitor.

Thicknesses of passive layers were estimated, based on the data listed in Table 3 resulting from fitting the experimental data to the equivalent circuit in Figure 8. The

capacitance of a constant phase element (CPE) in a parallel R-C circuit is given by (Hsu and Mansfield, 2001):

$$C = Y_0(i\omega_{max})^{n-1} \quad (37)$$

As stated by Frers (1990) and Martin et al. (2005), the overall capacitance C comprises the partial capacitances of the passive layer C_{ox} and the Helmholtz double layer C_H. Assuming a Helmholtz capacitance of 5×10^{-1} F m^{-2} (Frers, 1990) and given the electrode area of 3.53×10^{-5} m^2, the passive layer capacitance C_{ox} can be calculated:

$$\frac{1}{C_{ox}} = \frac{1}{C} - \frac{1}{C_H} = \frac{1}{C} - \frac{1}{1.765\times10^{-5}F} \quad (38)$$

This enables the estimation of the layer thickness d:

$$d = \frac{\varepsilon_r \cdot \varepsilon_0}{C_{ox}} \cdot A_e \quad (39)$$

where ε_0 denotes the vacuum permittivity (ε_0 = 8.854×10^{-12} F m^{-1}), ε_r the relative permittivity of aluminium oxide and A_e the electrode area. The value of the parameter ε_r was chosen as 10, based on values from the literature (Diggle and Ashok, 1976; Wolborski, 2005), though the permittivity of alumina (Al_2O_3) is extremely sensitive to its water content (Diggle and Ashok, 1976). A value of 4 was suggested for very dry γ-alumina powder, whereas Martin et al. (2005) used a value of 40 as the upper bound of their calculations for a partially hydrated passive layer. Furthermore, the permittivity also depends on the crystal structure with a value of bayerite reported as 9.4, whereas that for boehmite was measured as 20.5 (Diggle and Ashok, 1976). However, Bessone et al. (1983) used a permittivity of 9, whereas Hitzig et al. (1984) chose a value of 10. Thus, a permittivity of 10 is a reasonable estimate for a slightly hydrated oxide layer.

(Table 3 here)

Figure 9 shows a clear linear potential dependence of the layer thickness calculated for the aluminium electrode in sodium sulphate solution, as was already evident from the potential dependence of $-Z''_{max}$ values shown in Figure 7. Linear regression of the data in Figure 7 gave the following function:

$$d\,(\mathrm{nm}) = 1.9\ (\mathrm{nm\ V^{-1}}) \cdot \eta\,(\mathrm{V}) \qquad (40)$$

The estimated passivating layer thickness increased from about 0.8 nm at -1.0 V (SCE) to ca. 2.7 nm at -0.2 V (SCE), in agreement with reported values of 0.82 nm at -1.0 V (SCE) in 0.5 mol dm^{-3} NaCl (Frers, 1990), and 1 nm at -1.0 V (SCE) in 0.1 mol dm^{-3} NaCl (Martin et al., 2005), assuming a value of 40 for the relative permittivity of aluminium oxide. For a solution of 0.16 mol dm^{-3} ammonium tartrate, a growth coefficient of 0.75 nm V^{-1} has been reported (Bessone et al., 1983) (c.f. 1.9 nm V^{-1} from equation (40)), with thicknesses from 0.6 nm at -1.0 V (SCE) to 1.4 nm at -0.2 V (SCE), derived using a value of 10 for the relative permittivity of aluminium oxide.

In view of the uncertainties as to the nature of the interphase formed in humic acid and chloride containing solutions, and hence in permittivity values, effective layer thicknesses were not calculated from impedance data for such solutions.

4.3. Electrode Behaviour at Constant Current

Stationary aluminium electrodes were also used to characterise their behaviour under galvanostatic conditions. Surface preparation of the electrodes and their history, were found to have profound effects on their subsequent electrochemical behaviour. As mentioned above, electrodes were subjected to impedance measurements before and after the application of a constant current of ca. 3 A m^{-2}.

Figure 10 shows potential-time data for a smooth aluminium 1050 electrode with a constant current of 2.37 A m^{-2} in sodium sulphate solution with no pitting promoters

present, such as chloride; measurements were started immediately after the surface had been polished. Due to the growth of the passive layer on the electrode surface, the electrode potential rose linearly until the potentiostat's operational limit of the 10 V was reached. This suggests a linear growth of the passive layer; the rate of potential increase was ca. 0.054 V s^{-1}, as derived from the gradient of the line in Figure 10.

Figure 11 shows impedance spectra taken before and after oxidation for 600 seconds at 2.37 A m^{-2}. At a frequency of 8.3×10^{-2} Hz, the impedance increased from Z' = 13 and –Z'' = 27 Ω m^2 before the oxidation process to Z' = 80 and –Z'' = 260 Ω m^2 afterwards, due to thickening of the passive layer.

However, when the same electrode material was prepared with a rough surface finish (R_a = 1.041 µm) and immersed immediately in the same solution, very different potential-time data were measured, as shown in Figure 12. Over the first 70 seconds, the potential increased linearly, with a slightly smaller passivation rate (0.0165 V s^{-1}) than for the smooth electrode. However, the rate of increase of potential then decelerated, with a maximum potential of ca. 1.3 V (SCE) reached after ca. 75 s, followed by a dramatic decay in potential, which stabilised at about 0.3 V (SCE) after 400 s. This was an entirely spontaneous process, caused by the increased surface roughness of the electrode compared with the behaviour of the 'smooth' electrode resulting in the data in Figure 10, and with no pitting inducing chloride ions present in solution. Hitherto, only one recent publication has reported similar behaviour for aluminium electrodes, though in solutions containing high concentrations of sodium chloride and without providing a satisfactory explanation of this phenomenon (Mouedhen et al., 2008).

From the process engineering point of view, this spontaneous de-passivation under galvanostatic control is essential for the development of an effective electrocoagulation

process. It was observed for a large number of electrode types in different solutions, but with varying passivation times, rates and steady state potentials.

After the initial dissolution process, the electrode was subjected to re-passivation, by applying a constant potential of -0.55 V (SCE) for 30 minutes, which was followed by another dissolution process at constant current. The potential-time data after re-passivation (Figure 13) exhibited a very similar shape to that measured for a fresh electrode surface, but the electrode potential at the start was higher due to the increased passive layer thickness caused by re-passivation. After a short passivation period, in which a peak of 2.1 V (SCE) was reached at about 100 s, the potential decayed to a steady state value of ca. 0.3 V (SCE), demonstrating that spontaneous de-passivation was reversible and reproducible, even if the surface had been subject to re-passivation.

The galvanostatic behaviour of high purity electrodes was characterised, in addition to that of aluminium 1050. Figure 14 shows potential-time data for a smooth high purity aluminium electrode (R_a = 0.062 μm) during the application of a constant current density of 4.76 A m^{-2}. In contrast to the behaviour of the smooth, aluminium 1050 electrode (Figure 10), the potential increased sharply to a peak value of 1.5 - 1.8 V (SCE) over only a few seconds, but then decayed to a steady state value of ca. 0 V (SCE), due to spontaneous de-passivation. Thus, under these experimental conditions, high purity electrodes are to be preferred for electrocoagulation processes, being less prone to passivation than aluminium 1050.

Figure 15 shows impedance spectra acquired before and after oxidation at constant current density. The size of the semi-circle decreased significantly, implying a thinned passive layer. The increased depression of the post-oxidation semi-circle suggested increased surface roughness, as would be expected from an electrode surface that had undergone pitting dissolution.

In addition, the dissolution behaviour was investigated of electrodes that had been exposed to an aqueous environment at open-circuit (ca. -1.5 V (SCE)), to establish the effects of shut-down time on anodes in an electrocoagulation processes. Figure 16 shows potential-time data for a constant current density of 2.69 A m^{-2} at a rough, aluminium 1050 electrode (R_a = 1,340 μm) after it had been stored in a solution of 0.5 mol m^{-3} Na_2SO_4 for 72 hours, exhibiting passivation behaviour similar to that for a freshly prepared, smooth electrode, as shown in Figure 10. The same roughened electrode with a freshly prepared surface had previously exhibited spontaneous de-passivation, as indicated by Figure 12. Figure 16 shows a passivation rate of ca. 0.04 V s^{-1} for the first 35 seconds, similar to that of a smooth electrode, then it decelerated to a rate of 0.004 V s^{-1}, the cause of which is unclear; however, this would be congruous with the development of a more porous oxide outer layer. Apparently, hydrogen evolution and/or oxygen reduction under open circuit conditions enabled a gradual thickening of the passive layer, until it reached a critical thickness above which spontaneous de-passivation was completely inhibited, possibly due to hydrogen evolution producing hydroxide ions that dissolved the oxide film, as discussed in section 4.4.

Figure 17 shows that after the same rough aluminium 1050 electrode was stored in a solution of 0.5 mol m^{-3} Na_2SO_4 + 0.15 mol m^{-3} NaCl + 10 g m^{-3} humic acid for 72 hours, spontaneous de-passivation occurred, presumably due to the effects of chloride ions on the passive layer. The de-passivation profile was very similar to that exhibited for the same electrode with a freshly prepared surface; an initial passivation rate of ca. 0.04 V s^{-1} was observed for the first 30 seconds, at which the peak potential was 1.8 V (SCE), after which the potential decreased to a steady value of ca. 0.25 V (SCE).

554 Hence, even a relatively small concentration of chloride ions can trigger spontaneous
555 de-passivation by promoting pitting corrosion. It is likely that these ions were
556 incorporated into the passive film during electrode storage and thus were already
557 present when the dissolution process started inducing spontaneous de-passivation.

558 **4.4. Finite Element Reactor Scale Model**

559 A two-dimensional model of the distribution of ionic and particulate species in a typical
560 bench-scale electrocoagulation reactor was developed in Comsol Multiphysics®,
561 version 3.4 (Modelling Guide, www.comsol.com). As outer boundary, a reactor with a
562 rectangular structure of 0.002×0.15 m^2 was defined with an anode producing Al^{3+} ions
563 by reaction (1) and a cathode evolving hydrogen by reaction (2). The homogeneous
564 precipitation by reactions (4) and (5) was included, taking kinetic data from the
565 literature (Holmes et al., 1968). The following three sets of equations were solved
566 simultaneously:

567 i) 'Navier-Stokes' simulating laminar fluid flow at 10 dm^3 $hour^{-1}$ with the physical
568 properties of water at 298 K:

569 $$\rho\frac{\partial\vec{u}}{\partial t}-\nabla\left[\eta\left(\nabla\vec{u}+(\nabla\vec{u})^T\right)\right]+\rho\left(\vec{u}\cdot\nabla\right)\vec{u}+\nabla p=\vec{F} \qquad (41)$$

570 ii) 'Nernst-Planck' simulating the distribution of the ionic species, i, Al^{3+}, $Al(OH)^{2+}$,
571 Na^+, SO_4^{2-}, H^+ and OH^-:

572 $$\nabla\cdot\left(-D_i\nabla c_i-z_i u_{m,i}Fc_i\nabla\phi\right)+\vec{u}\nabla c_i=R_i \qquad (42)$$

573 iii) 'Convection and diffusion' simulating the distribution of the suspended $Al(OH)_3$
574 particles, formed with reaction rate *R*:

575 $$\nabla\cdot\left(-D\nabla c+c\vec{u}\right)=R \qquad (43)$$

In an attempt to further explain the observed spontaneous de-passivation, the finite element model was used to predict the spatial distribution of ions in a continuous electrocoagulation reactor with parallel plate electrodes.

The 'homogeneous' precipitation of aluminium forming $Al(OH)_3$ in two steps, as outlined in section 2, was assumed to have first order kinetics. A value of 10^5 s^{-1} (Holmes et al., 1968) was used for the kinetic rate coefficient k_1 for reaction (4). No value for the rate coefficient k_2 for reaction (5) could be found in the literature, so 10^4 s^{-1} was chosen, considering the increased size of the reactant compared to the previous reaction and hence the increased probability of slower reaction kinetics. Equilibrium constants for these reactions were determined from thermodynamic data (Perrault, 1985).

An influx of water with pH 7 flowing at 2.78×10^{-6} m^3 s^{-1} (equivalent to 10 dm^3 h^{-1} or a single phase Re = 150) was applied to the model reactor, together with an anode potential of 0.4 V (SHE) or 0.155 V (SCE), which resulted in a calculated current density of 14.3 A m^{-2}. No effect of passivation was taken into account. Kinetic data for the electrochemical dissolution of aluminium (Hurlen et al., 1984) and hydrogen evolution (Dražić and Popić, 1993) reactions were taken from the literature.

Figure 18 shows the two-dimensional spatial distribution of pH in the reactor, generated by solving equations (41) to (43) using the finite element method. The pH of ca. 5.5 near the anode, due to reactions (5) and (6) releasing protons, decayed with distance to the bulk (influx) solution value of 7, from which it increased to ca. 12 near the cathode, due to hydrogen evolution by reaction (2) producing OH^- ions. Figure 2b predicts that a pH of ca. 5.5 would enable spontaneous dissolution of $Al(OH)_3$ as $\left[Al_{13}O_4\left(OH\right)_{24}\right]^{7+}$ ions.

600 The low pH at the anode facilitates aluminium dissolution, dissolving pre-existing oxide
601 and postponing aluminium hydrolysis and (hydrous)oxide formation, which occurs
602 progressively as Al^{3+} ions are transported towards the bulk solution mainly by
603 convective diffusion. This explains the relatively low steady state electrode potential
604 and feasibility of electrocoagulation process for influents with neutral pH, at which
605 Figure 1 predicts passivation.

606 **5. Conclusions**

607 Aluminium tends to passivate in neutral electrolyte solutions, resulting in very small
608 dissolution current densities over a wide potential range. It was shown that the thickness
609 of the passive layer grows linearly with increasingly positive electrode potentials. The
610 presence of natural contaminants, such as humic acid, exacerbates the problem, which is
611 detrimental to the performance of electrocoagulation reactors, for which a constant
612 dosage of dissolved aluminium(III) and a minimal energy demand is required. However,
613 the effects of passivation can be diminished by adding pitting promoters, such as
614 chloride ions, to the electrolyte solution, though such chemical additions would increase
615 the complexity and costs of electrocoagulation processes, so are not the preferred option
616 to achieve performance improvements.

617 In the experiments reported here, a constant current was applied that caused a smooth
618 aluminium electrode to exhibit passivation behaviour resulting in a constantly
619 increasing anode potential, cell voltage and hence specific electrical energy
620 consumption, threatening the technical and economic viability of any electrocoagulation
621 process. However, when the electrode surface was roughened, the electrode potential
622 decreased dramatically to a low and steady value. This effect of 'spontaneous de-
623 passivation' was observed even without the presence of chloride ions. Exposing the
624 electrode at open circuit to an electrolyte solution for long times reversed the effect. It

625 can be attributed to the hydrolysis of dissolved aluminium(III) ions close to the
626 electrode surface releasing protons, which dissolve the pre-existing passive layer and
627 enhance dissolution rates. Apparently, this dissolution process is facilitated by cracks in
628 the passivating layer of the rough electrode surface.

629 Hence, contrary to common perception, it is possible to dissolve aluminium
630 electrochemically at neutral pH without the addition of pitting promoters just by simply
631 roughening the electrode surface. It can be concluded that the electrocoagulation
632 treatment of natural waters containing none or very low concentrations of chloride just
633 requires a freshly roughened aluminium electrode surface, which may improve the
634 technical and economic viability of electrocoagulation processes significantly. Further
635 research is still required to better understand the process of spontaneous de-passivation.

636 **Acknowledgements**

637 The authors thank Yorkshire Water, Bradford (UK), for funding this project.

638

References

Adhikari, S., Ai, J., Hebert, K.R., Ho, K.M., Wang, C.Z., 2010. Hydrogen in aluminium during alkaline corrosion. Electrochimica Acta 55 (19), 5326-5331.

Adhikari, S., Hebert, K.R., 2008. Participation of aluminium hydride in the anodic dissolution of aluminium in alkaline solutions. Journal of The Electrochemical Society 155 (5), C189-C195.

Adhikari, S., Lee, J., Hebert, K.R., 2008. Formation of aluminium hydride during alkaline dissolution of aluminium. Journal of The Electrochemical Society 155 (1), C16-C21.

Azumi, K., Ueno, T., Seo, M., 2004. Cathodic dissolution behaviour of an aluminium wire electrode in solutions containing borate and sulphate ions. Journal of Electroanalytical Chemistry 567 (1) 1-7.

Baes, C.F. Jr., Mesmer, R.E., 1976. The Hydrolysis of Cations, Wiley, New York.

Bereket, G., Yurt, A., 2001. The inhibition effect of amino acids and hydroxy carboxylic acids on pitting corrosion of aluminium alloy 7075. Corrosion Science 43 (6), 1179-1195.

Bessone, J., Mayer, C., Jüttner, K., Lorenz, W.J., 1983. AC-impedance measurements on aluminium barrier type oxide films. Electrochimica Acta 28 (2), 171-175.

Billik, P., Horváth, B., 2008. Mechanochemical synthesis of the $[Al_{13}O_4(OH)_{24}(H_2O)_{12}]^{7+}$ Keggin ion. Inorganic Chemistry Communications 11 (10), 1125-1127.

Boisier, G., Portail, N., Pébère, N., 2010. Corrosion inhibition of 2024 aluminium alloy by sodium decanoate. Electrochimica Acta 55 (21), 6182-6189.

Bottero, J.Y., Cases, J.M., Fiessinger, F., Poirier, J.E., 1980. Studies of hydrolyzed aluminium chloride solutions. 1. Nature of aluminium species and composition of aqueous solutions. Journal of Physical Chemistry 84 (22), 2933-2939.

Boukamp, B.A., 2004. Electrochemical impedance spectroscopy in solid state ionics: recent advances. Solid State Ionics 169 (1-4), 65-73.

Brown, O.R., Whitley, J. S., 1987. Electrochemical behaviour of aluminium in aqueous caustic solutions. Electrochimica Acta 32 (4), 545-556.

Can, O.T., 2006. Treatment of the textile wastewater by combined electrocoagulation. Chemosphere 62, 181-187.

671 Carmona, M., Khemis, M., Leclerc, J-P., Lapicque, F., 2006. A simple model to predict
672 the removal of oil suspensions from water using the electrocoagulation technique.
673 Chemical Engineering Science. 61, 1237-1246.
674 Chen, X. Chen, G., Yue, P.L., 2002. Investigation on the electrolysis voltage of
675 electrocoagulation. Chemical Engineering Science 57, 2449 – 2455.
676 Diggle, J.W., Ashok, K.V., 1976. Oxides and Oxide Films, Marcel Dekker, New York.
677 Dražić, D., Popić, J., 1993. Hydrogen evolution on aluminium in chloride solutions.
678 Journal of Electroanalytical Chemistry 357 (1-2), 105-116.
679 Frers, S.E., 1990. AC-Impedance measurements on aluminum in chloride containing
680 solution and below the pitting potential. Journal of Applied Electrochemistry 20 (6),
681 996-999.
682 Guseva, O., Schmitz, P., Suter, T., von Trzebiatowski, O., 2009. Modelling of anodic
683 dissolution of pure aluminium in sodium chloride. Electrochimica Acta 54 (19),
684 4514-4524.
685 Heusler, K.E., Allgaier, W., 1971. Die kinetik der aufloesung von aluminium in
686 alkalischen loesungen. Werkstoffe und Korrosion 4, 297 - 302.
687 Hitzig, J., Jüttner, K., Lorenz, W.J., Paatsch, W., 1984. AC-Impedance measurements
688 on porous aluminium oxide films. Corrosion Science 24 (11-12), 945-952.
689 Holmes, L.P., Cole, D.L., Eyring, E.M., 1968. Kinetics of aluminium ion hydrolysis in
690 dilute solutions. The Journal of Physical Chemistry 72 (1), 301 - 304.
691 Holt, P.K., Barton, G.W., Mitchell, C.A., 2004. Deciphering the science behind
692 electrocoagulation remove suspended clay particles from water. Water Science &
693 Technology 50 (12), 177-184.
694 Hsu, C.H., Mansfeld, F., 2001. Technical note: Concerning the conversion of the
695 constant phase element parameter Y-0 into a capacitance. Corrosion 57 (9), 747-748.
696 Hurlen, T., Haug, A.T., 1984. Corrosion and passive behaviour of aluminium in weakly
697 alkaline solution. Electrochimica Acta 29 (8), 1133-1138.
698 Hurlen, T., Lian, H., Ødegard, O.S., 1984. Corrosion and passive behaviour of
699 aluminium in weakly acid solution. Electrochimica Acta 29 (5), 579-585.
700 Jiang, J.Q., Graham, N.J.D., Kelsall, G.H., Brandon, N.P., 2002. Laboratory study of
701 electro-coagulation-flotation for water treatment. Water Research 36, 4064-4078.
702 Jüttner, K., Lorenz, W.J., 1989. The role of surface inhomogeneities in corrosion
703 processes. Electrochemical impedance spectroscopy (EIS) on different aluminum-
704 oxide films. Corrosion Science 29 (2-3), 279-288.

Khemis, M., 2005. Electrocoagulation for the treatment of oil suspensions relation between the rates of electrode reactions and the efficiency of waste removal. Process Safety and Environmental Protection 83(B1), 50-57.

Kobya, M., 2003. Treatment of textile wastewaters by electrocoagulation using iron and aluminum electrodes. Journal of Hazardous Materials 100, 163-178.

Kumar, P.R., 2004. Removal of arsenic from water by electrocoagulation. Chemosphere 55, 1245-1252.

Lee, W.J., 2000. Effects of sulphate ion additives on the pitting corrosion of pure aluminium in 0.01 M NaCl solution. Electrochimica acta 45 (12), 1901-1910.

Lin, C-F., Porter, M.D., Hebert, K.R., 1994. Surface films produced by cathodic polarization of aluminium. Journal of The Electrochemical Society 141 (1), 96-104.

Lin, Y-F., Lee, D-J., 2010. Purification of aluminium tridecamer salt using organic solvent precipitation. Separation and Purification Technology 75 (2), 218-221.

Martin, F.J., Cheek, G.T., O'Grady, W.E., Natishan, P.M., 2005. Impedance studies of the passive film on aluminium. Corrosion Science 47 (12), 3187-3201.

Mouedhen, G., Feki, M., De Petris Wery, M., Ayedi, H.F. 2008. Behavior of aluminum electrodes in electrocoagulation process. Journal of Hazardous Materials 150 (1), 124-135.

Ogle, K., Serdechnova, M., Mokaddem, M., Volovitch, P., 2011. The cathodic dissolution of Al, Al2Cu, and Al alloys. Electrochimica Acta 56 (4), 1711-1718.

Parga, J.R. Cocke, D. L., Valenzuela, J.L., Gomes, J.A., Kesmez, M., Irwin, G., Moreno, H., Weir, M., 2005. Arsenic removal via electrocoagulation from heavy metal contaminated groundwater in La Comarca Lagunera Mexico. Journal of Hazardous Materials 124, 247-254.

Pébère, N., Boisier, G., 2008. EIS study of sealed AA2024 anodized in sulphuric acid solutions. 213th Meeting of the Electrochemical Society, Phoenix, AZ, 18-23 May 2008, The Electrochemical Society, Abstract 906.

Perrault, G.G., 1979. The role of hydrides in the equilibrium of aluminium in aqueous solutions. Journal of the Electrochemical Society 126 (2), 199-204.

Perrault, G. G., in Bard, A.J., Parsons R., Jordan, J. (Eds.), 1985. Standard Potentials in Aqueous Solutions, Marcel Dekker, New York, pp.555-580.

Qiu, C., Olson, G.B., Opalka, S.M., Anton, D.L., 2004. Thermodynamic evaluation of the Al-H system. Journal of Phase Equilibria and Diffusion 25 (6), 520-527.

738 Szklarska-Smialowska, Z., 1986. Pitting Corrosion of Metals, National Association of
739 Corrosion Engineers, Houston, TX.
740 Takahashi, H., Fujiwara, K., Seo, M., 1994. The cathodic polarization of aluminium
741 covered with anodic oxide films in a neutral borate solution – II. Film breakdown
742 and pit formation. Corrosion Science 36 (4), 689-705.
743 Vik, E.A., Carlson, D. A., Eikum, A.S., Gjessing, E.T. 1984. Electrocoagulation of
744 potable water. Water Research 18 (11), 1355-1360.
745 Wolborski, M., 2005. Characterization of aluminum and titanium oxides deposited on
746 4H SiC by atomic layer deposition technique. Materials Science Forum 483, 701-
747 704.
748

Tables

Figure Captions

Figure 1. Superimposed potential-pH diagrams for Al-H_2O at 298 K considering stable Al_2O_3(c) and (dashed lines) meta-stable $Al(OH)_3$ (amorphous); dissolved Al^{III} activity = 10^{-4}.

Figure 2. a) pH dependence of Al_2O_3(c) solubility in equilibrium with Al^{III} species at 298 K.

b) pH dependence of $Al(OH)_3$ (amorphous) solubility in equilibrium with Al^{III} species at 298 K.

Figure 3. Potential-pH diagram for Al-H_2O considering Al_2O_3 (c) at 298 K; dissolved aluminium activity = 10^{-4}; superimposed stability regions of (i) AlH_3 and AlH^{2+} (dashed lines) (ii) AlH_3 / Al^{III} (dotted line) if AlH^{2+} does not exist.

Figure 4. Tafel plot of a linear potential sweep of a high purity aluminium disc in 0.5 mol m^{-3} Na_2SO_4; start potential: -2.3 V (SCE), end potential: 0.5 V (SCE), scan rate 1 mV s^{-1}, rotation rate: 2000 rpm.

Figure 5. Cyclic voltammogram of a high purity aluminium disc in a) 0.5 mol m^{-3} Na_2SO_4 + 0.4 mol m^{-3} NaCl, b) 0.5 mol m^{-3} Na_2SO_4 + 0.4 mol m^{-3} NaCl + 5 g m^{-3} humic acid, c) 0.5 mol m^{-3} Na_2SO_4 + 0.4 mol m^{-3} NaCl + 10 g m^{-3} humic acid, d) 0.5 mol m^{-3} Na_2SO_4 ; start potential: -2.1 V (SCE), vertex potential: 0.0 V (SCE), end potential: -2.1 V (SCE), scan rate 10 mV s^{-1}, rotation rate: 80 rpm.

Figure 6. Nyquist plots of electrochemical impedance of aluminium 1050 in a) 0.5 mol m^{-3} Na_2SO_4 , b) 0.5 mol m^{-3} Na_2SO_4 + 10 g m^{-3} humic acid, c) 0.5 mol m^{-3} Na_2SO_4 + 10 g m^{-3} humic acid + 0.15 mol m^{-3} NaCl; ● -0.2 V (SCE), x -0.6 V (SCE), ○ -1.0 V (SCE).

Figure 7. Maximum imaginary impedance –Z''max as function of electrode potential; Δ 0.5 mol m^{-3} Na_2SO_4, x 0.5 mol m^{-3} Na_2SO_4 + 10 g m^{-3} humic acid, ○ 0.5 mol m^{-3} Na_2SO_4 + 10 g m^{-3} humic acid + 0.15 mol m^{-3} NaCl.

785 Figure 8. Equivalent analogue electrical circuit in which (R_1 and CPE_1) and (R_2 and
786 CPE_2) correspond respectively to porous outer and underlying barrier oxide
787 layers, and R_e represents electrolyte resistance.

788 Figure 9. Calculated passive layer thickness as function of electrode potential on
789 aluminium Al1050 in 0.5 mol m^{-3} Na_2SO_4.

790 Figure 10. Time dependence of potential of 'smooth' aluminium 1050 electrode in 0.5
791 mol m^{-3} Na_2SO_4; constant current density: 2.37 A m^{-2}.

792 Figure 11. Nyquist plot of electrochemical impedance spectra of 'smooth' aluminium
793 1050 electrode in 0.5 mol m^{-3} Na_2SO_4; x before the dissolution process, ○
794 after the dissolution process, inset: impedance values at frequencies of ca. 1
795 Hz.

796 Figure 12. Time dependence of electrode potential of 'rough' aluminium 1050
797 electrode in 0.5 mol m^{-3} Na_2SO_4; constant current density: 2.69 A m^{-2}.

798 Figure 13. Time dependence of electrode potential of 'rough' aluminium 1050
799 electrode in 0.5 mol m^{-3} Na_2SO_4 for a fresh surface and after 30 minutes at a
800 constant potential E = -0.55 V (SCE); constant current density: 2.69 A m^{-2}.

801 Figure 14. Time dependence of electrode potential of **'**smooth' high purity aluminium
802 electrode in 0.5 mol m^{-3} Na_2SO_4; constant current density: 4.76 A m^{-2}.

803 Figure 15. Nyquist plot of electrochemical impedance spectra of 'smooth' high purity
804 aluminium electrode in 0.5 mol m^{-3} Na_2SO_4; ○ before the dissolution
805 process, x after oxidation at 4.76 A m^{-2} for 600 s.

806 Figure 16. Electrode potential as function of time of electrode 'rough' aluminium 1050
807 electrode in 0.5 mol m^{-3} Na_2SO_4 after being stored in solution for 72 hours;
808 constant current density: 2.69 A m^{-2}.

809 Figure 17. Electrode potential as function of time of electrode 'rough' aluminium 1050
810 electrode in 0.5 mol m^{-3} Na_2SO_4 + 10 g m^{-3} humic acid + 0.15 mol m^{-3} NaCl
811 after being stored in solution for 72 hours; constant current density: 2.69 A
812 m^{-2}.

Figure 18. Predicted pH-profile in an electrocoagulation reactor; anode: aluminium dissolution, cathode: hydrogen evolution, flow rate: 10^{-2} m^3 h^{-1}, inter-electrode gap: 2 mm, electrode length: 140 mm, electrode width: 35 mm.

Figure 1
Click here to download Figure: Figures_1.pdf

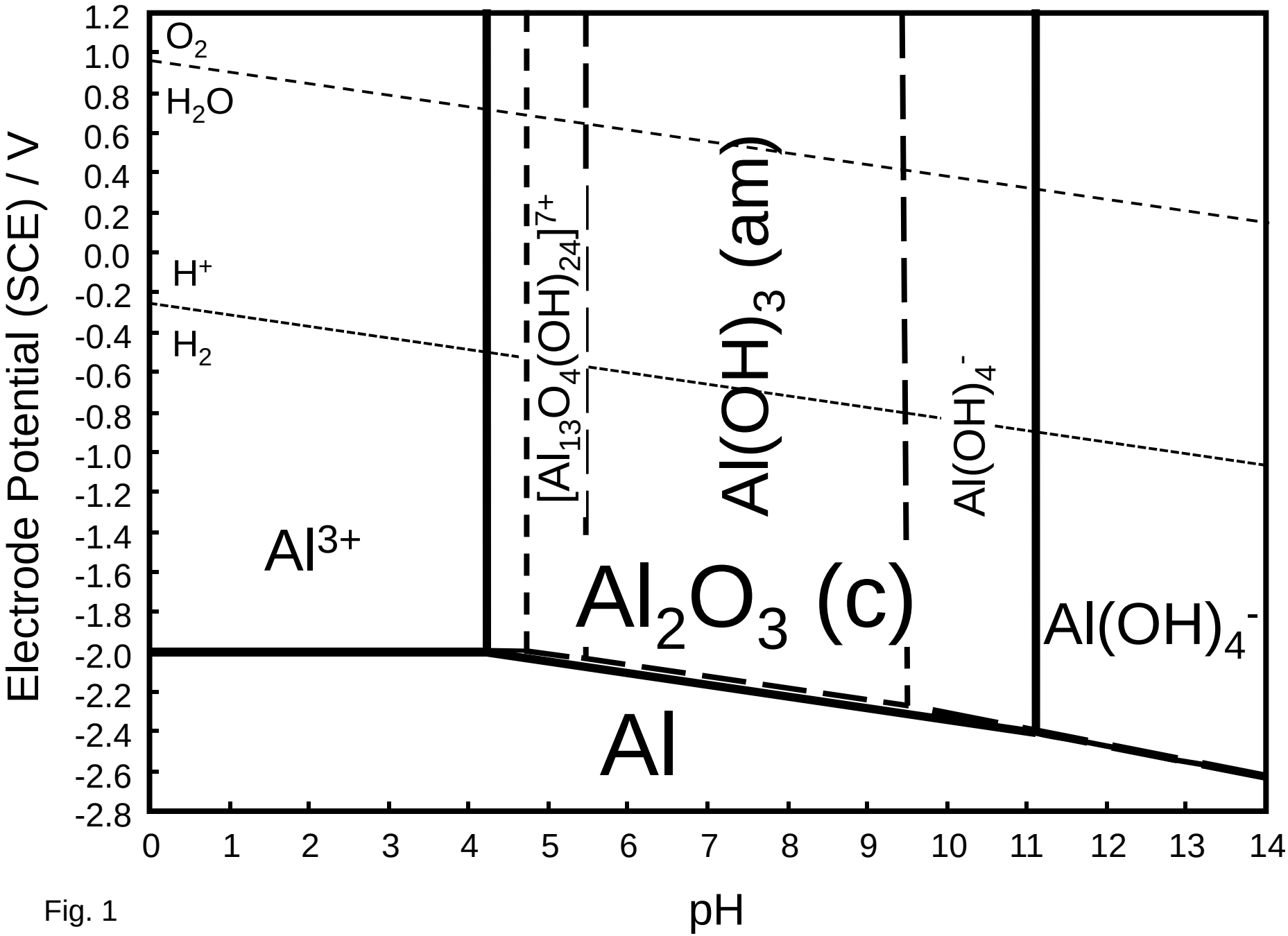

Fig. 1

Figure 2a
Click here to download Figure: Figures_2a.pdf

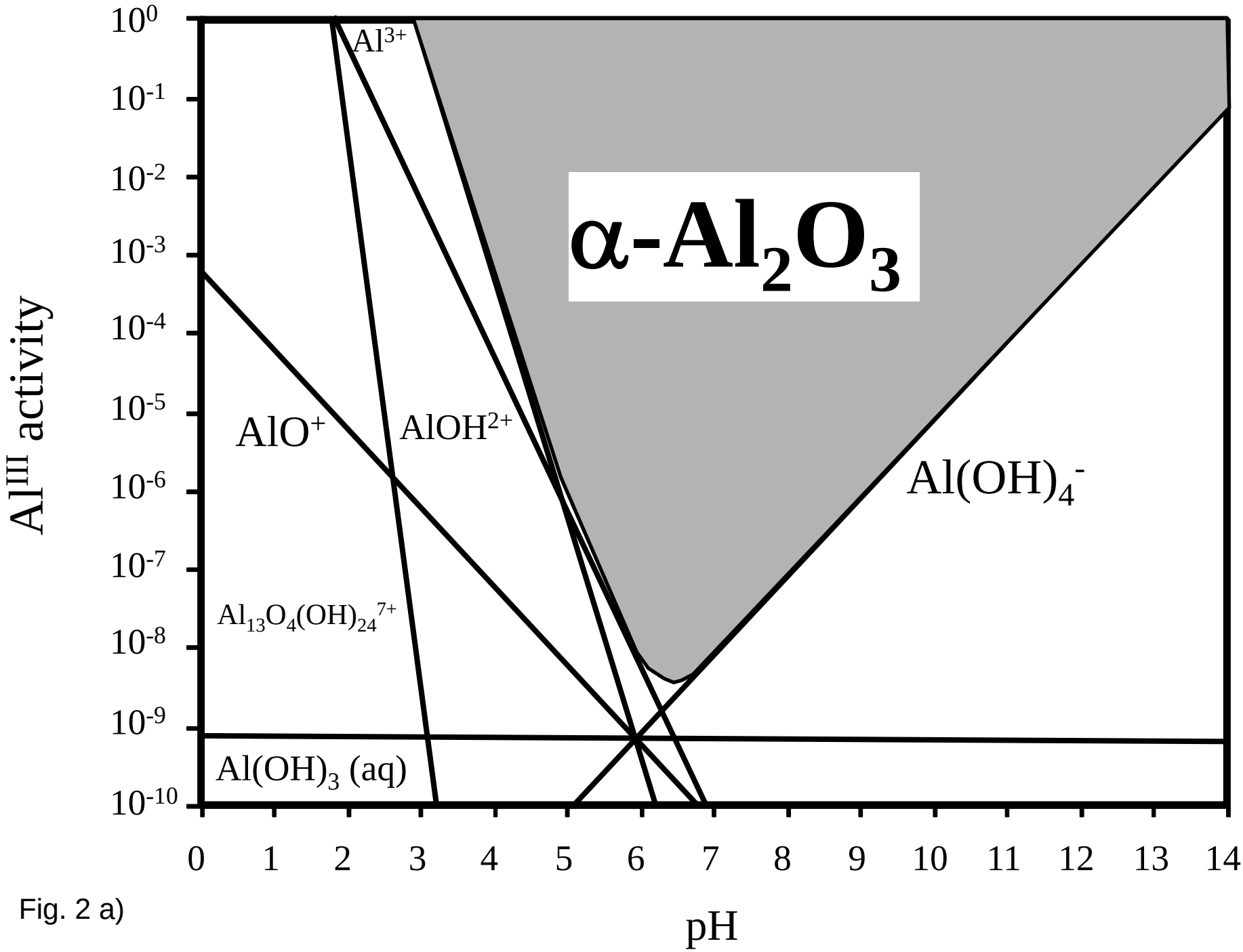

Fig. 2 a)

Figure 2b

Click here to download Figure: Figures_2b.pdf

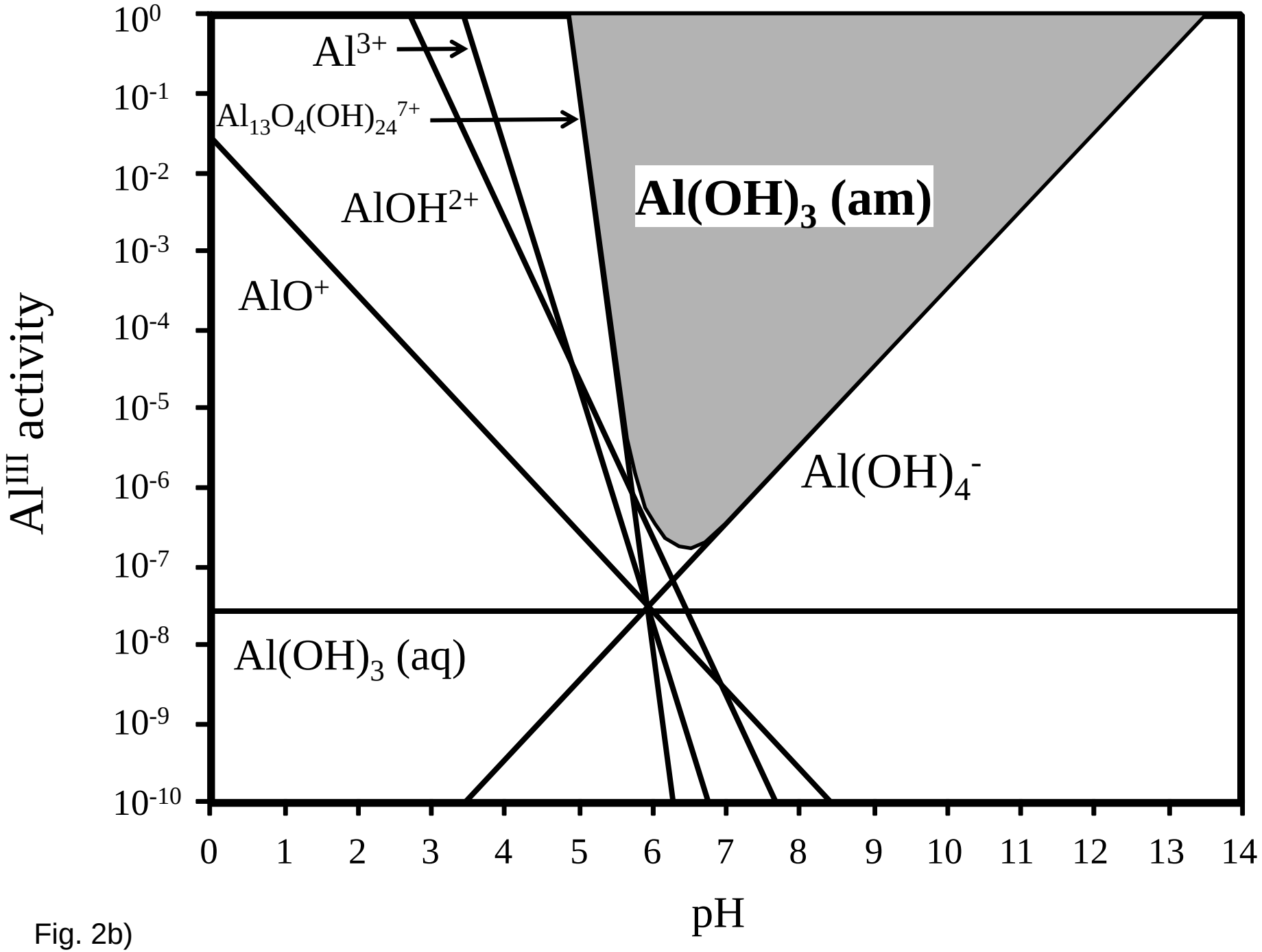

Fig. 2b)

Figure 3
Click here to download Figure: Figures_3.pdf

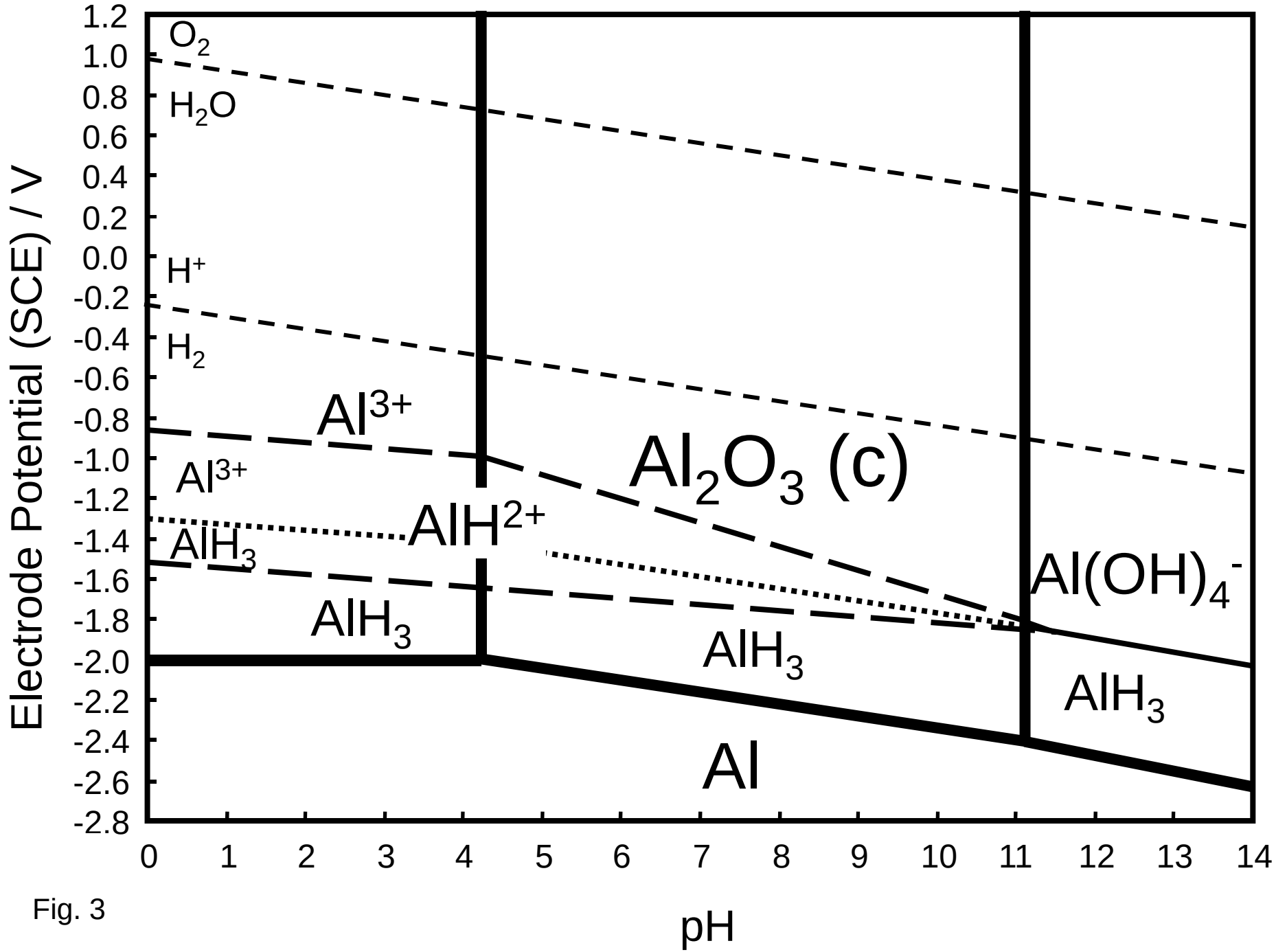

Fig. 3

Figure 4
Click here to download Figure: Figures_4.pdf

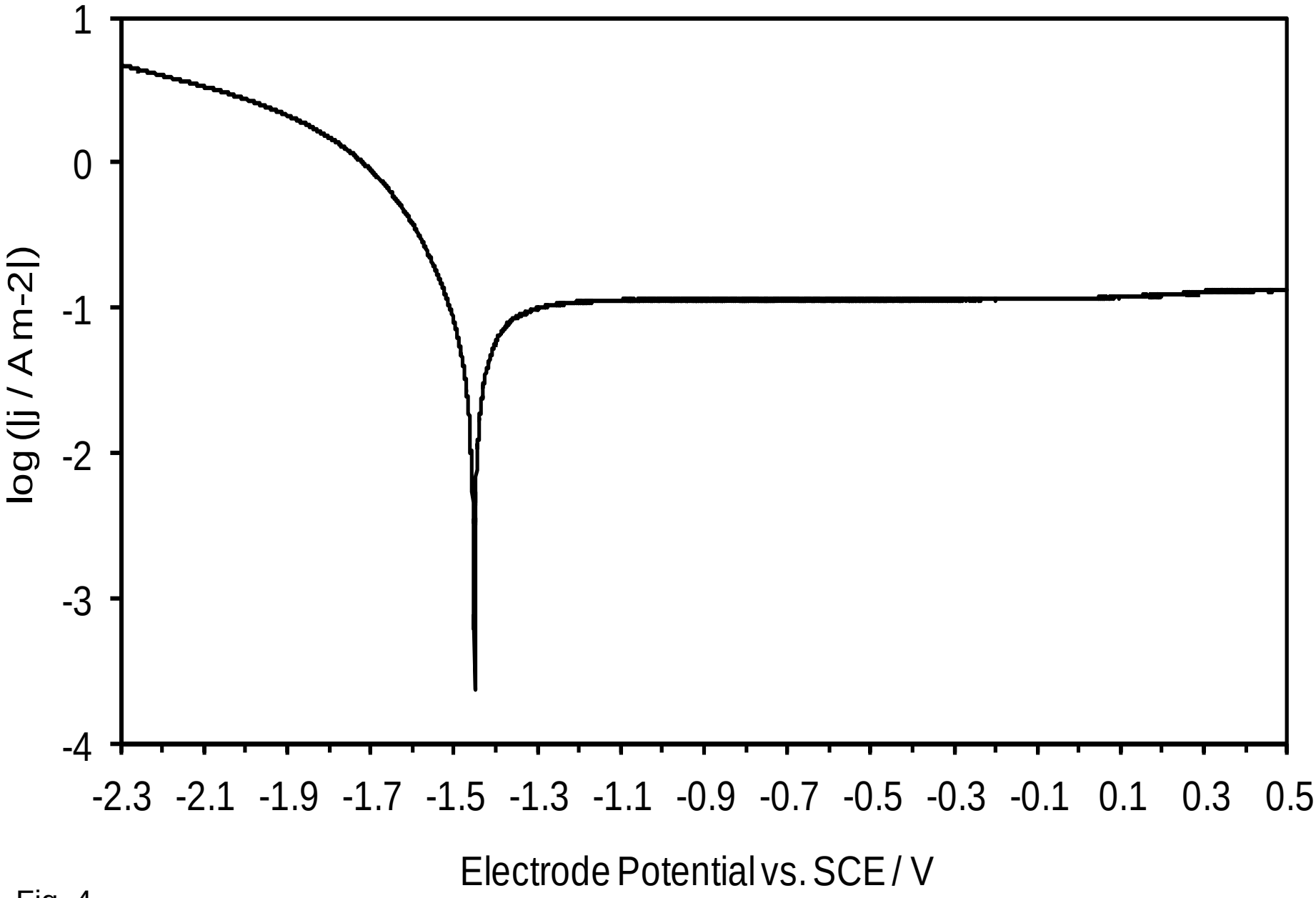

Fig. 4

Figure 5

Click here to download Figure: Figures_5.pdf

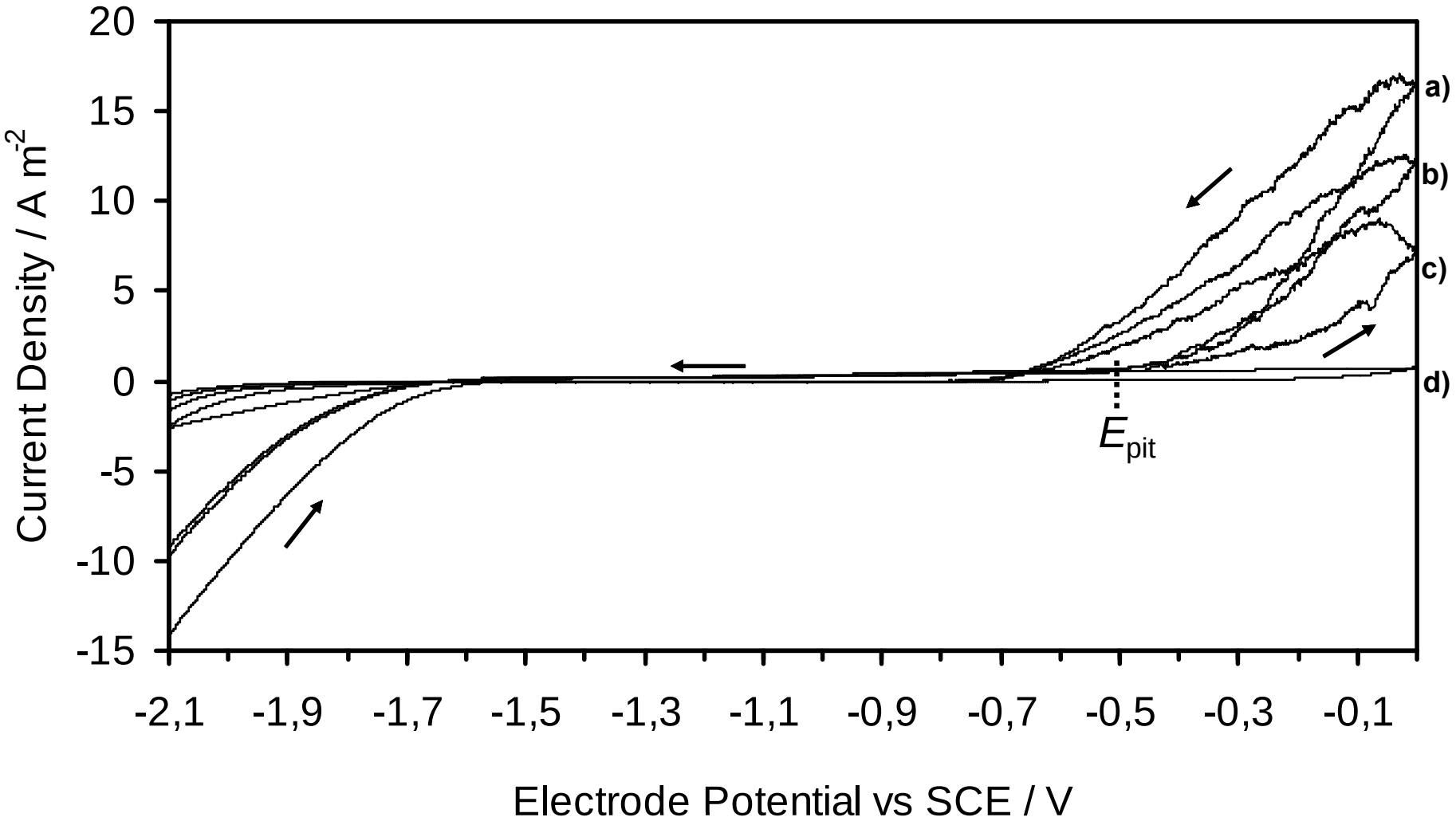

Fig. 5

Figure 6a

Click here to download Figure: Figures_6a.pdf

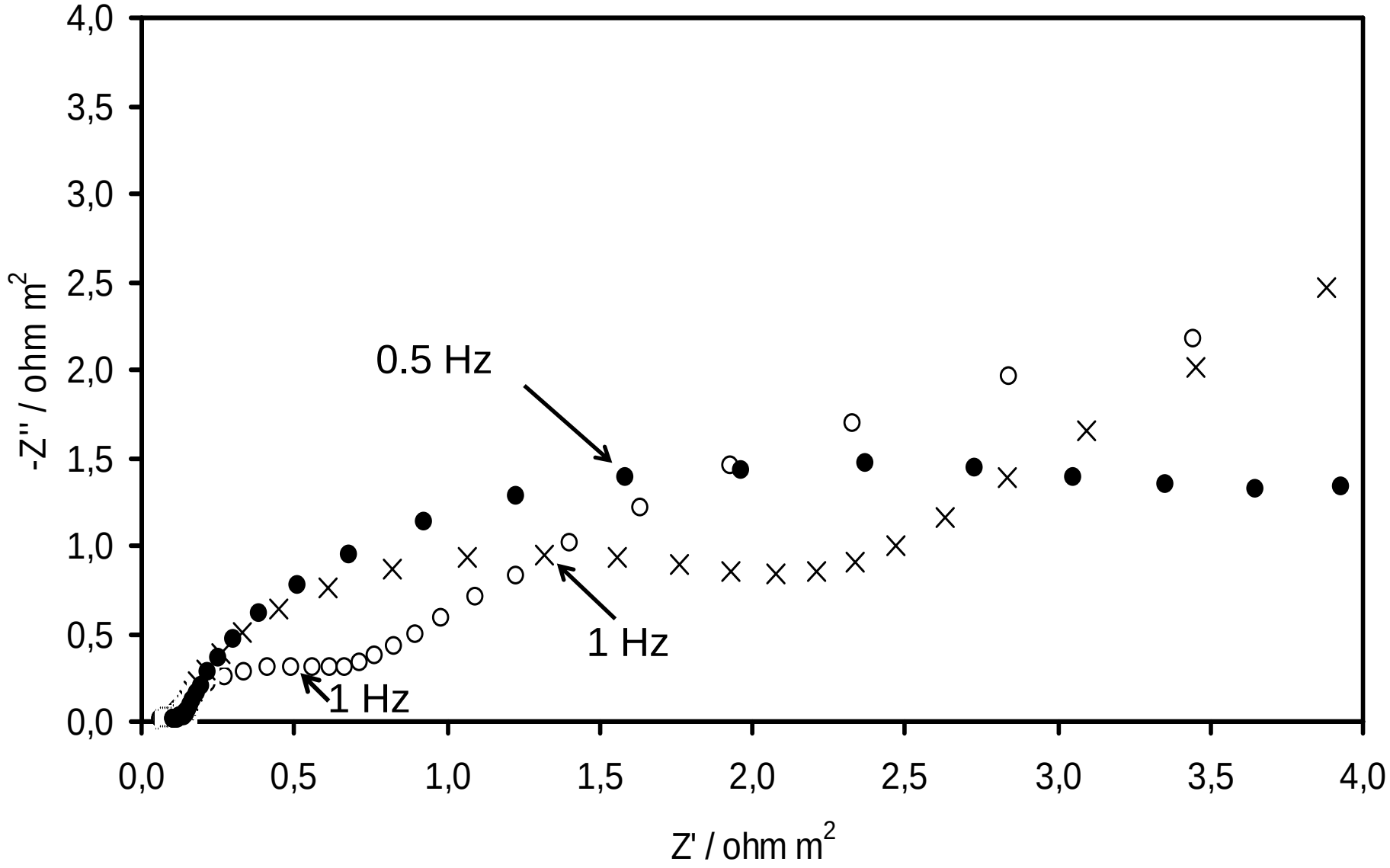

Fig. 6 a)

Figure 6b

Click here to download Figure: Figures_6b.pdf

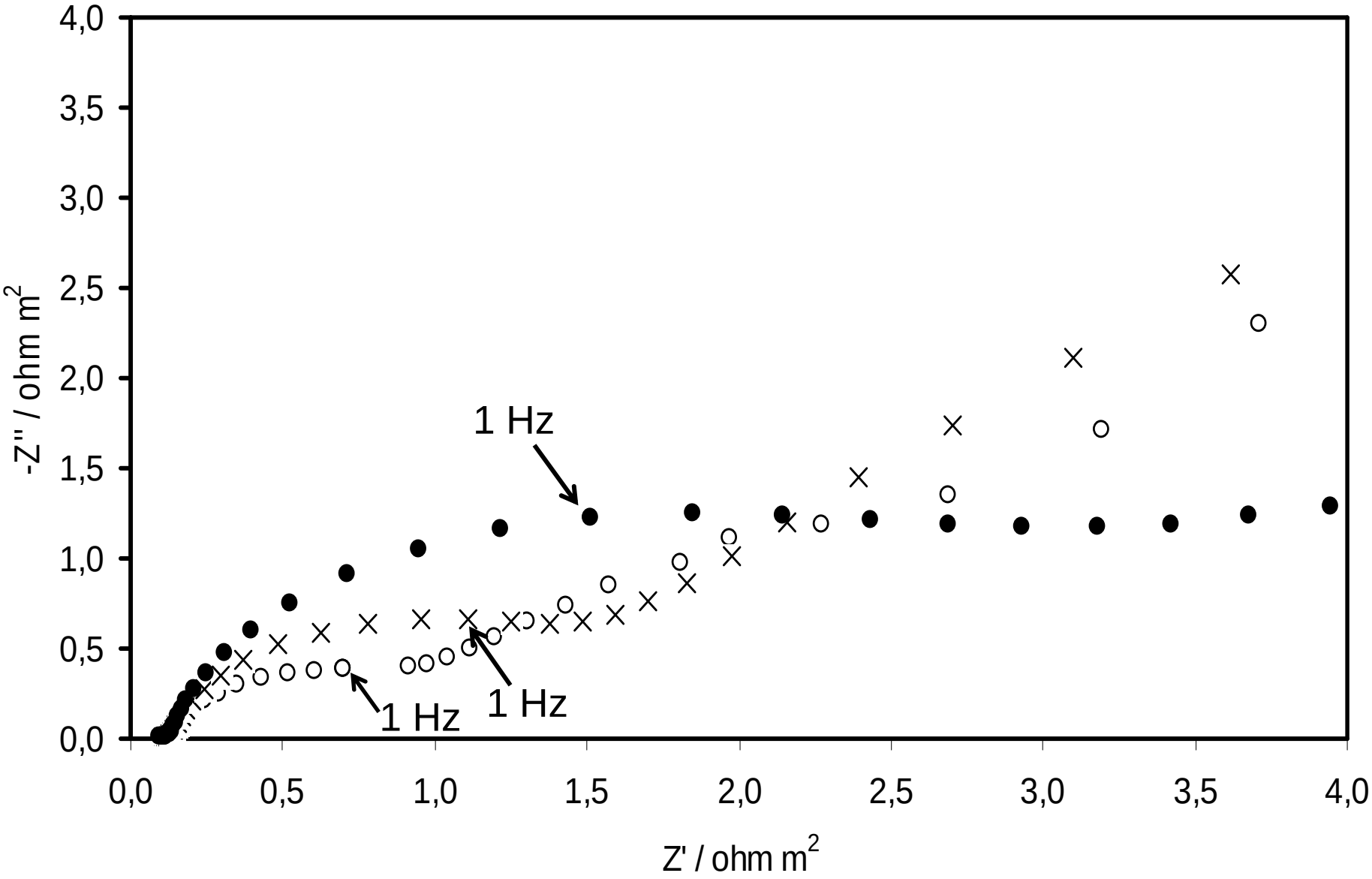

Fig. 6b)

Figure 6c
Click here to download Figure: Figures_6c.pdf

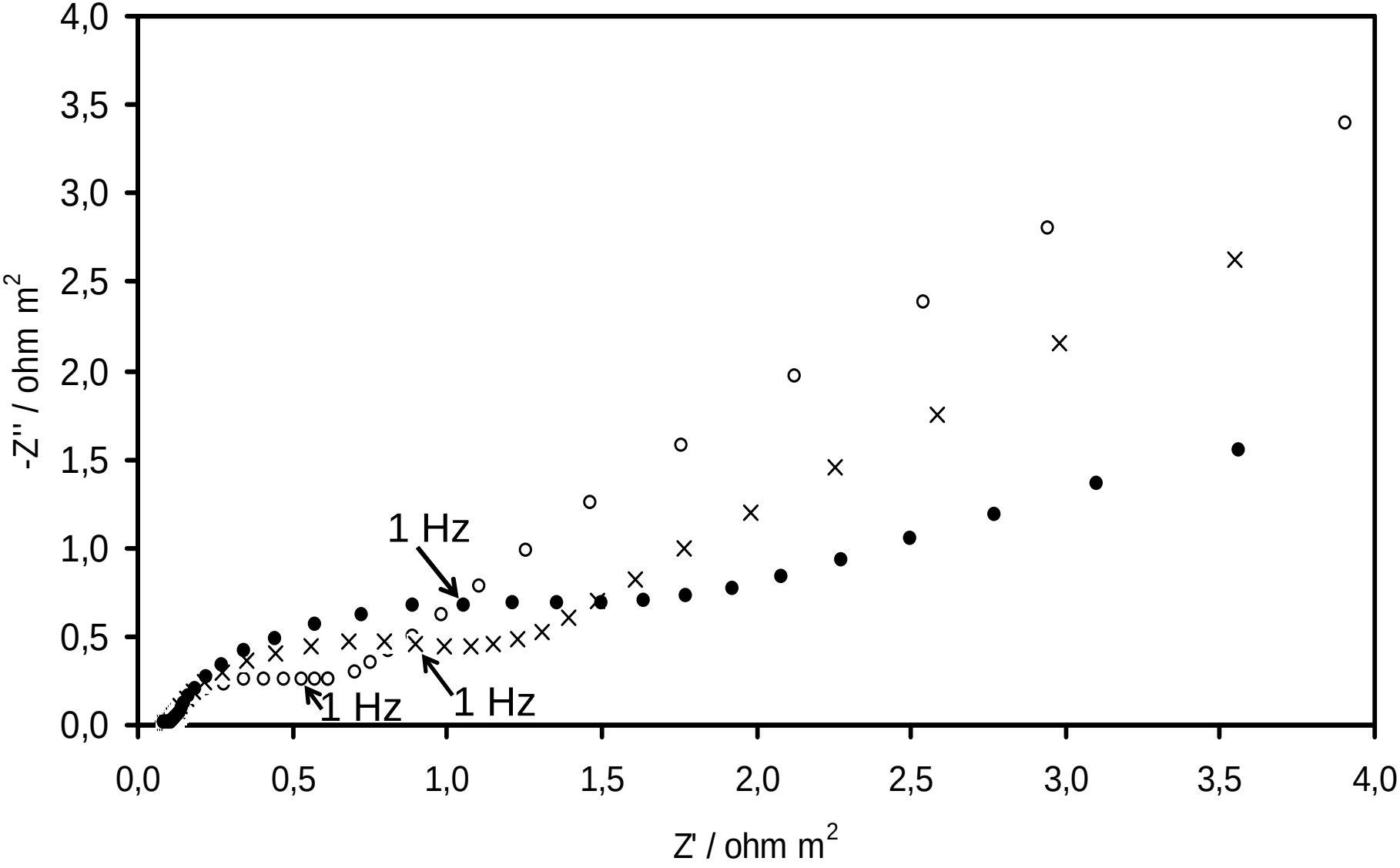

Fig. 6 c)

Figure 7
Click here to download Figure: Figures_7.pdf

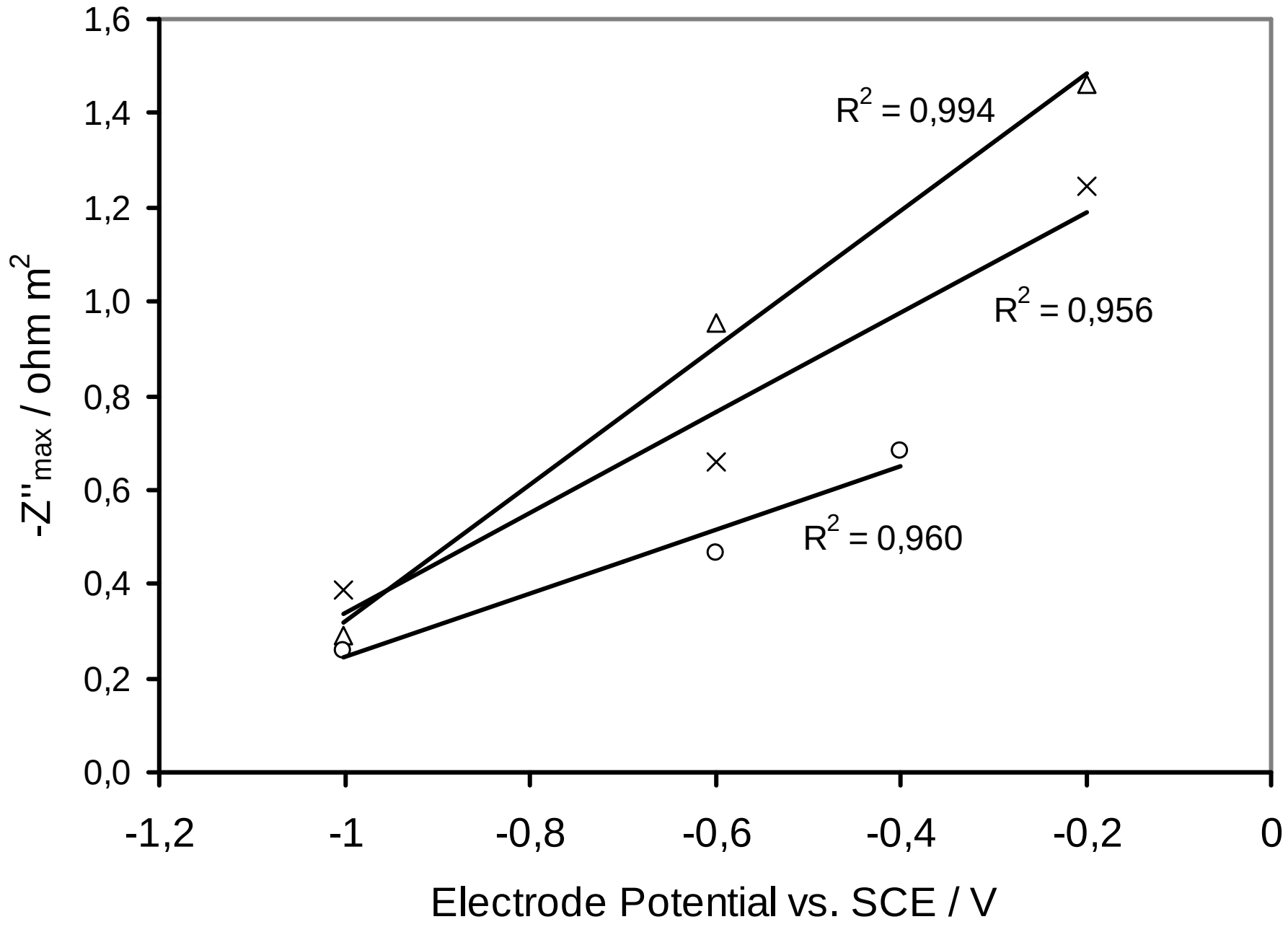

Fig. 7

Figure 8
Click here to download Figure: Figures_8.pdf

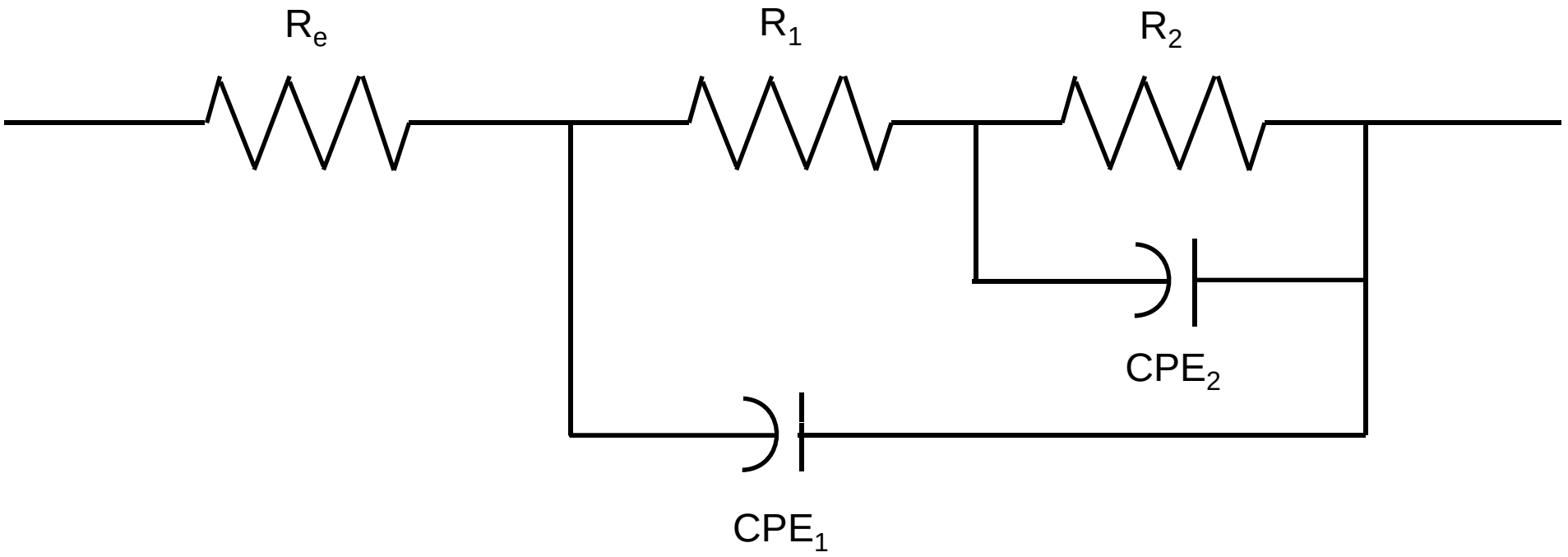

Fig. 8

Figure 9
Click here to download Figure: Figures_9.pdf

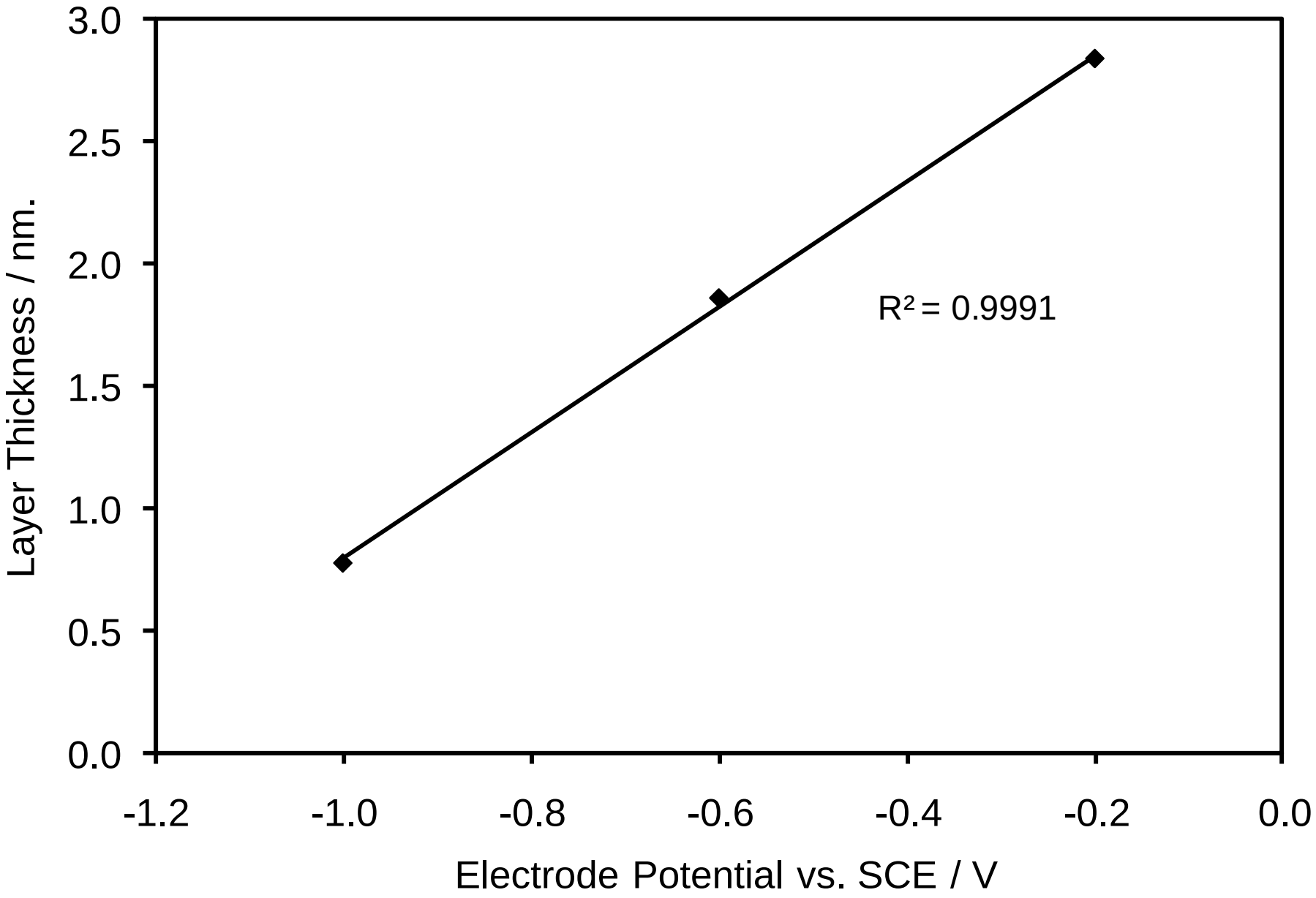

Fig. 9

Figure 10

Click here to download Figure: Figures_10.pdf

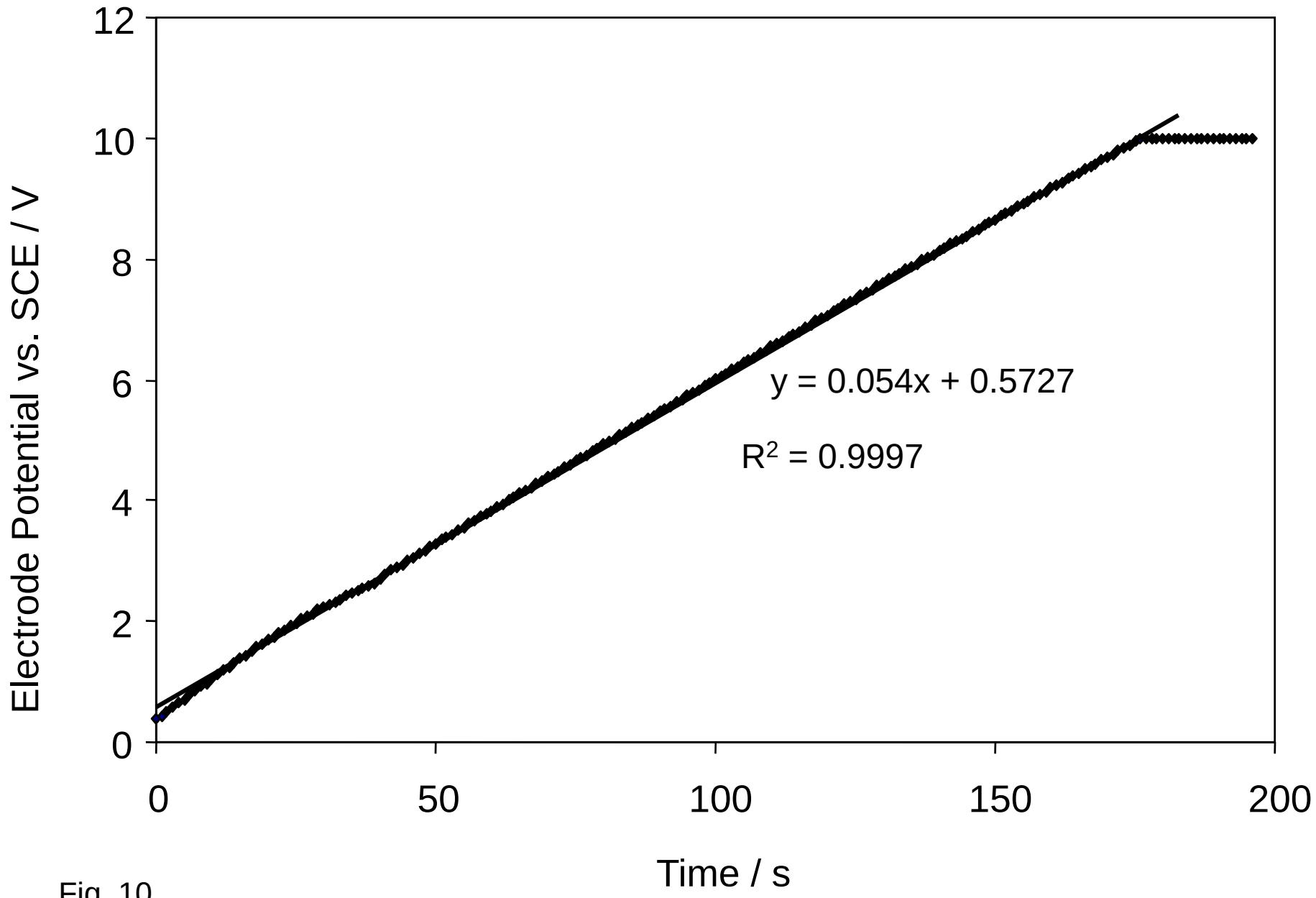

Fig. 10

Figure 11

Click here to download Figure: Figures_11.pdf

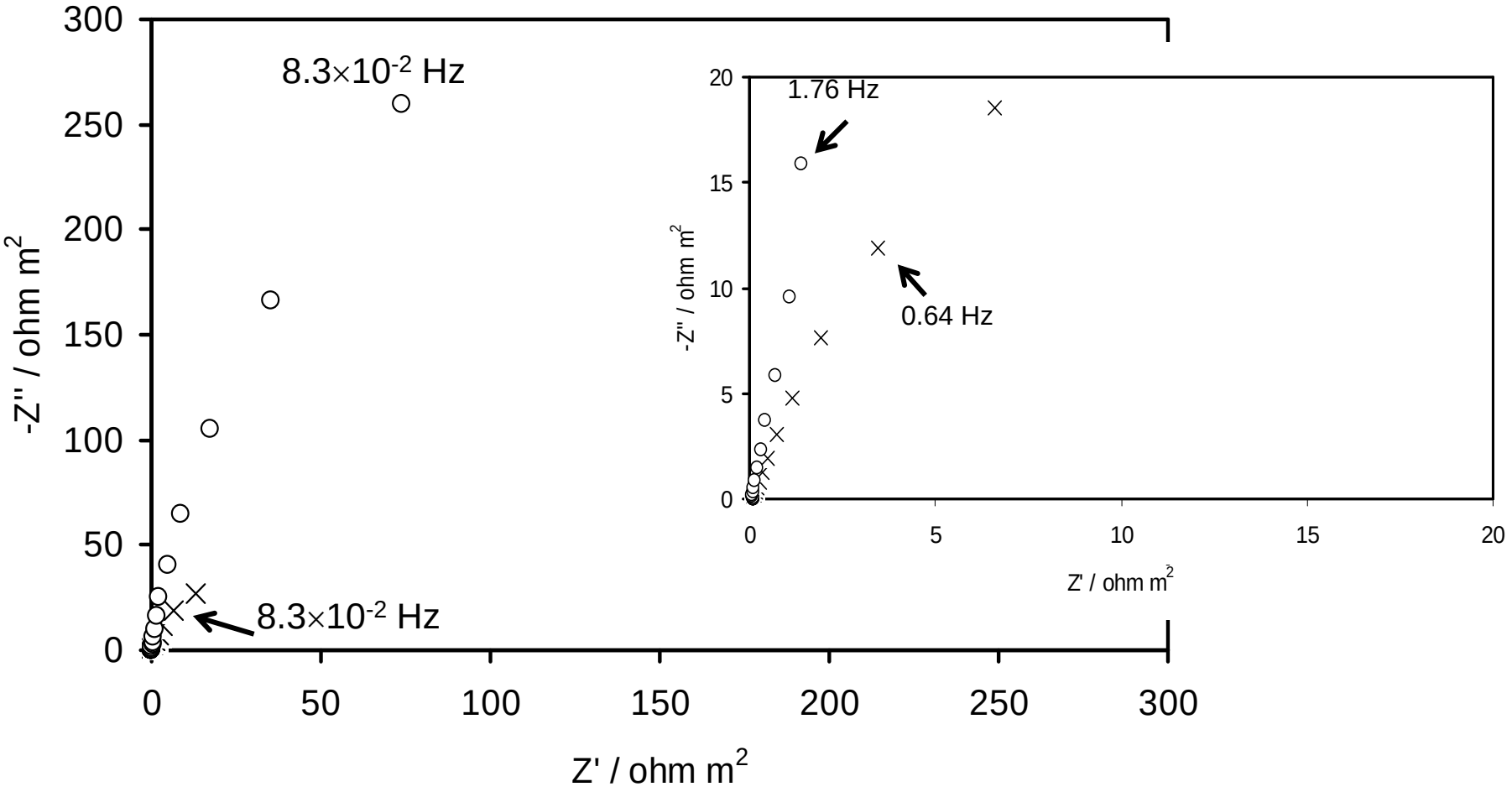

Fig. 11

Figure 12
Click here to download Figure: Figures_12.pdf

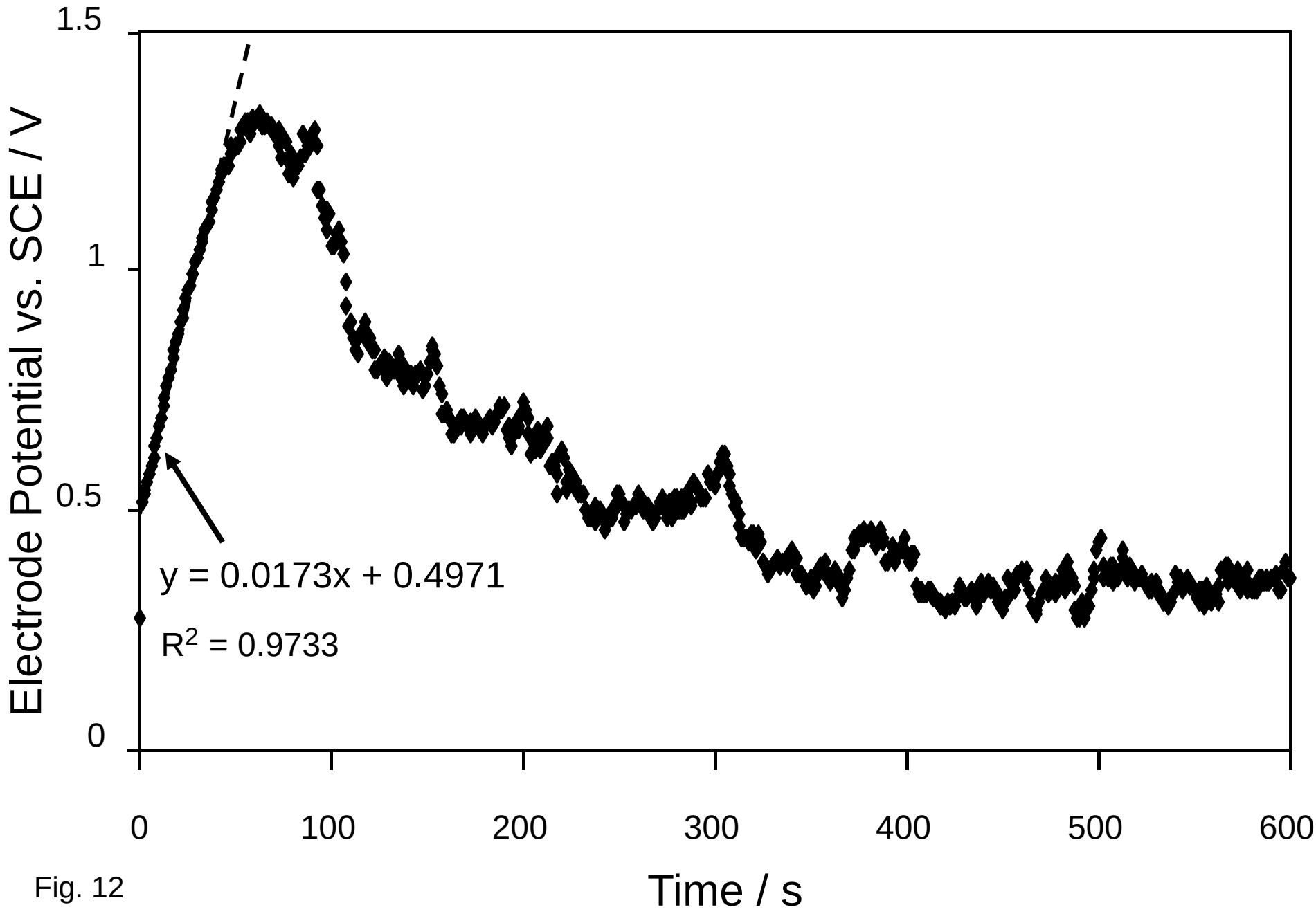

Fig. 12

Figure 13
Click here to download Figure: Figures_13.pdf

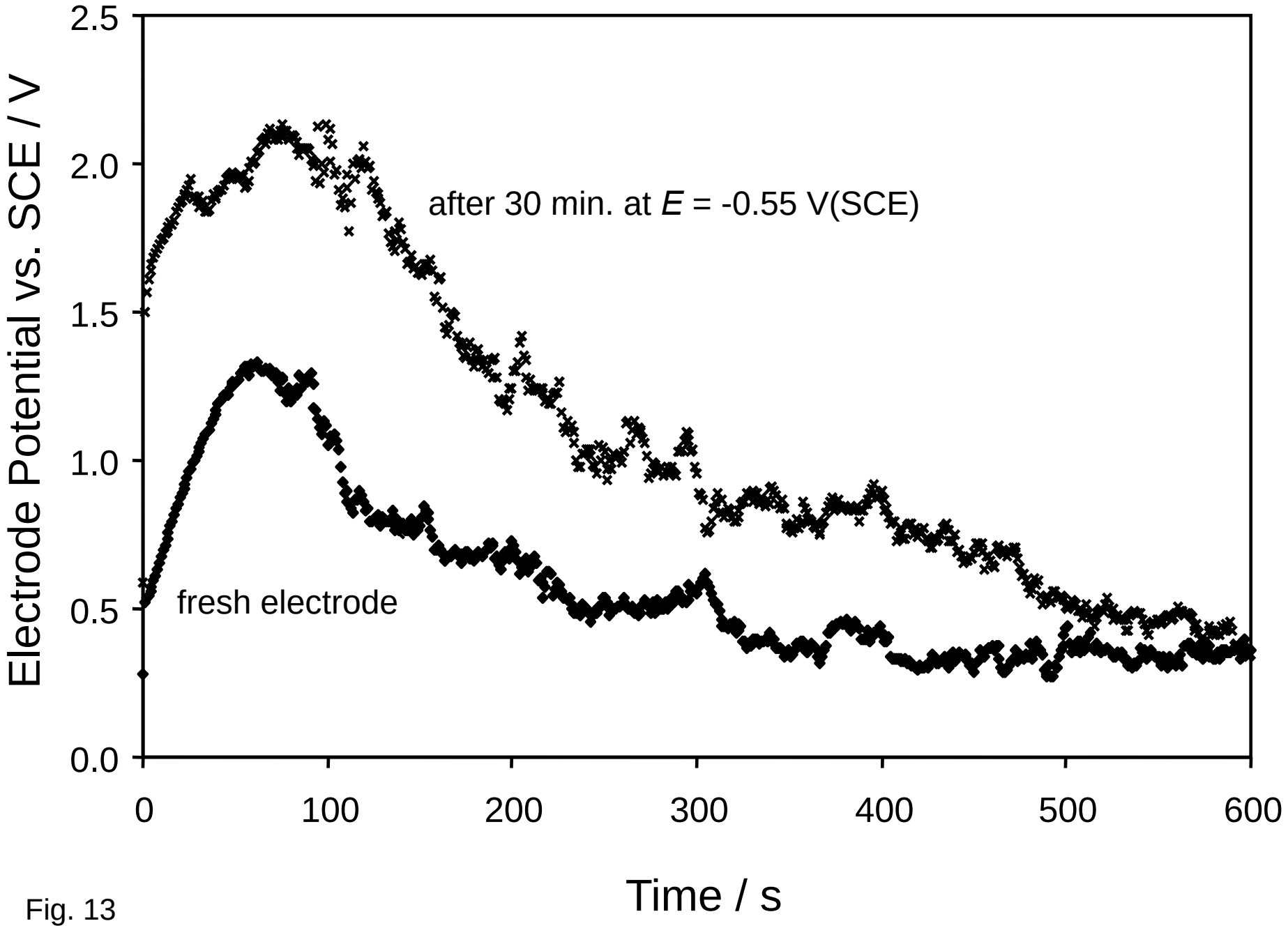

Fig. 13

Figure 14
Click here to download Figure: Figures_14.pdf

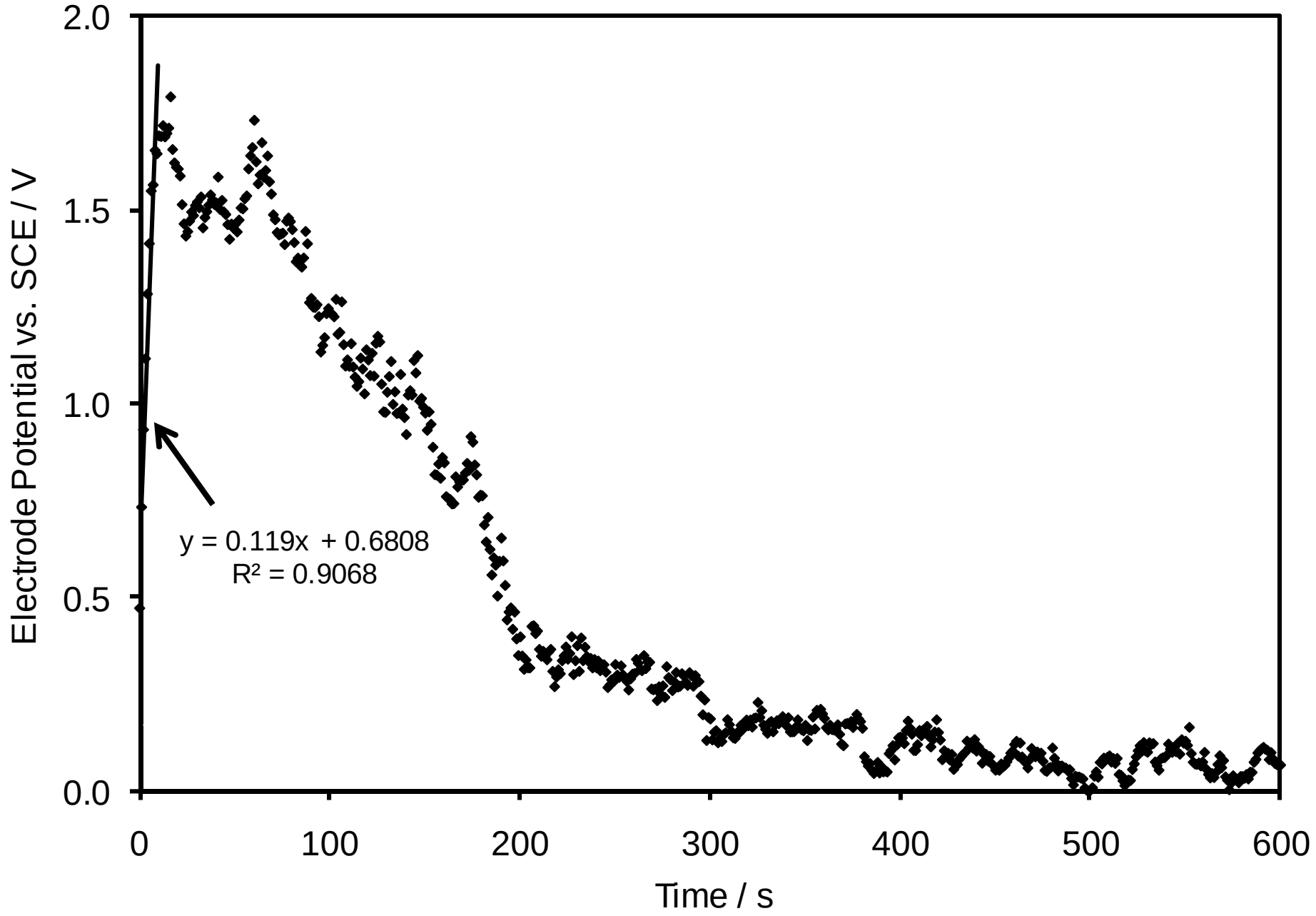

Fig. 14

Figure 15
Click here to download Figure: Figures_15.pdf

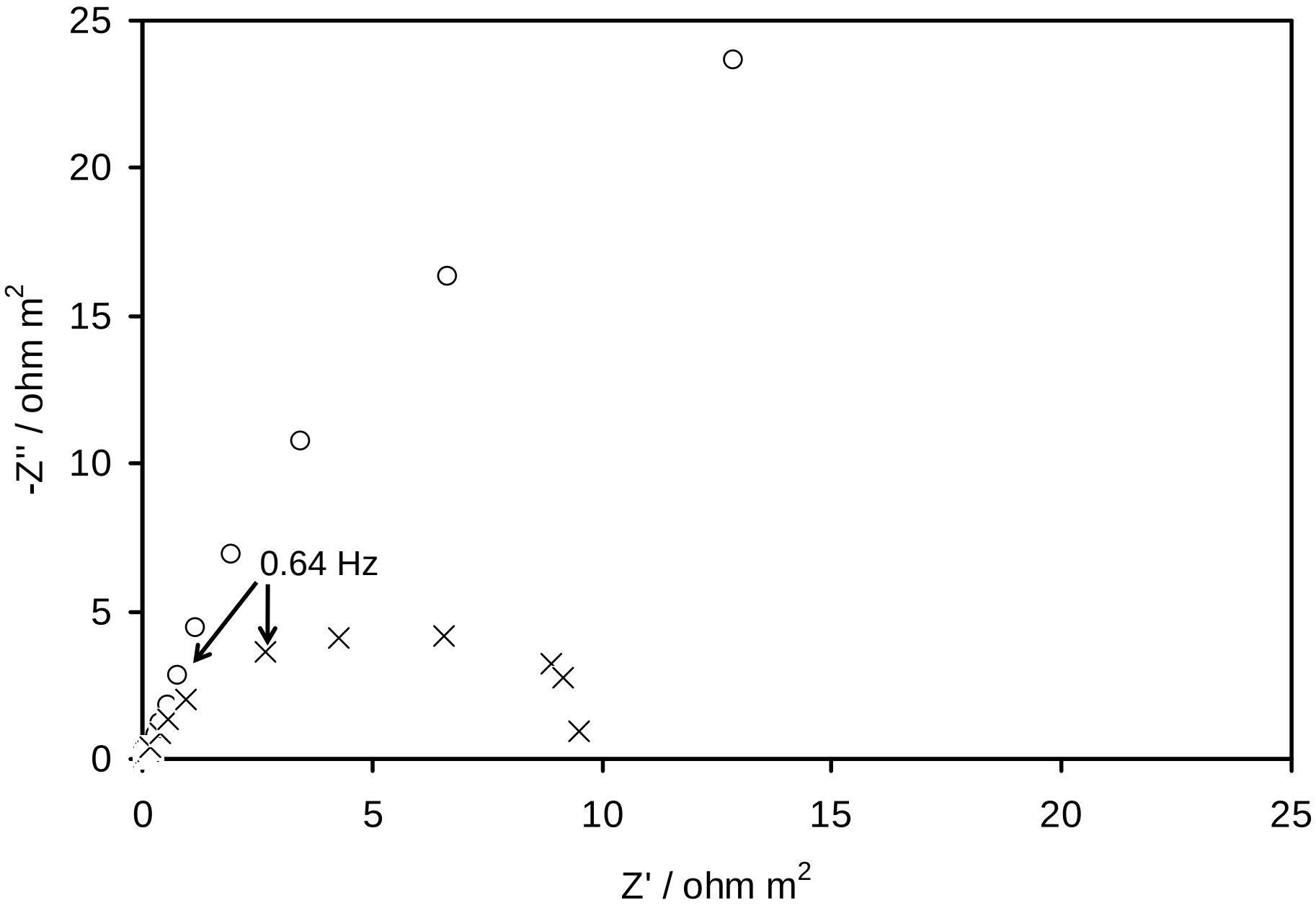

Fig. 15

Figure 16
Click here to download Figure: Figures_16.pdf

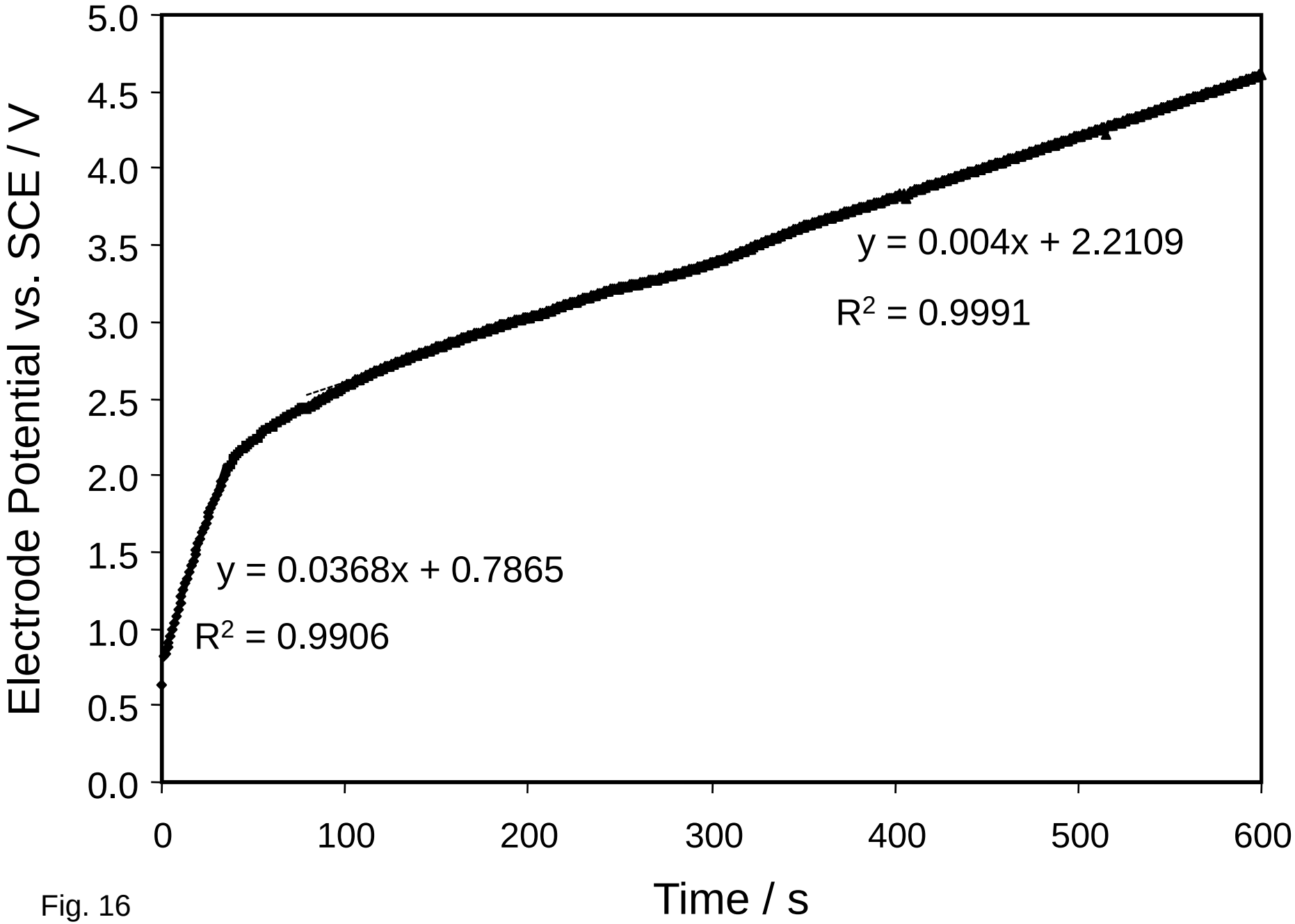

Fig. 16

Figure 17
Click here to download Figure: Figures_17.pdf

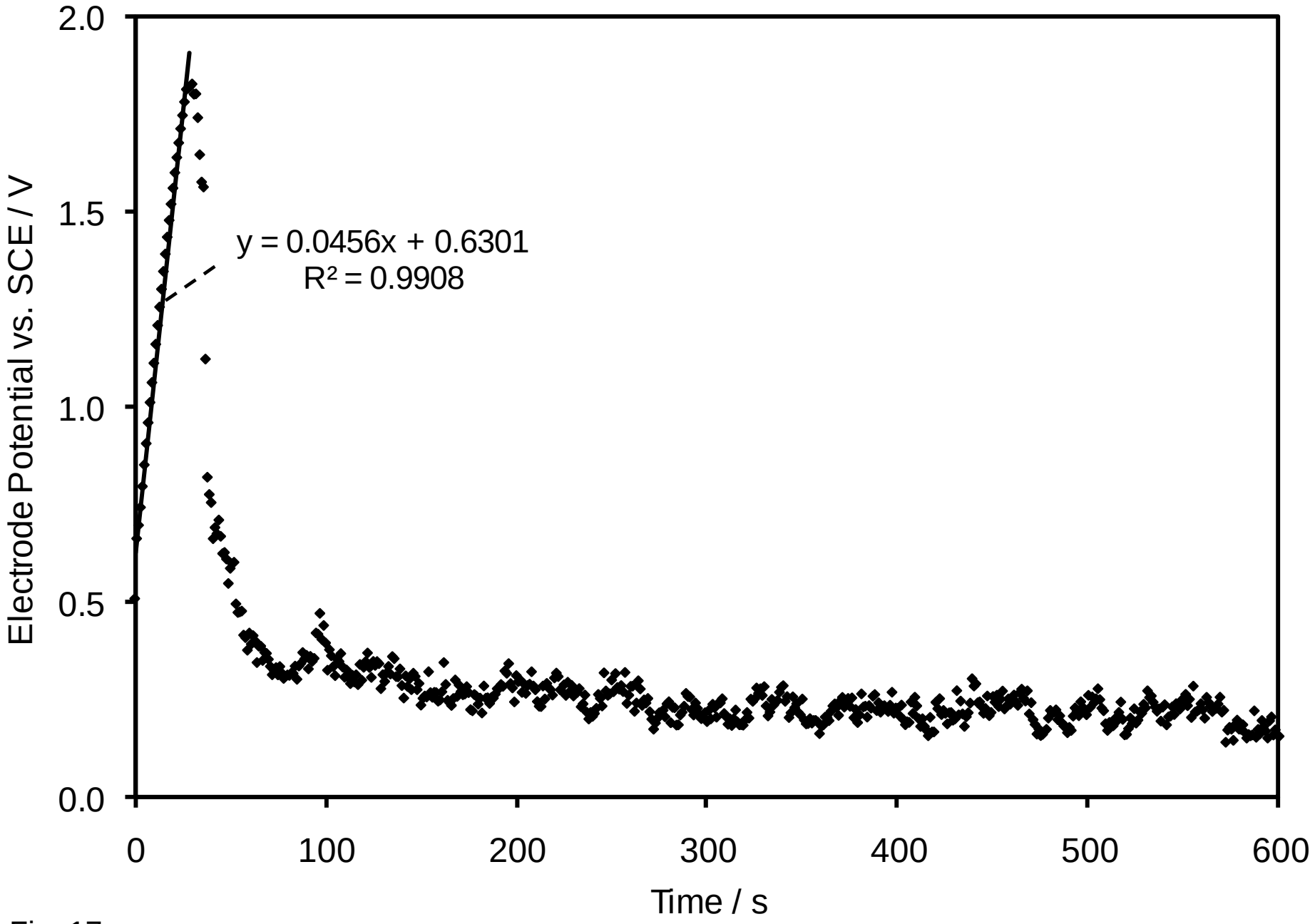

Fig. 17

Figure 18
Click here to download Figure: Figures_18.pdf

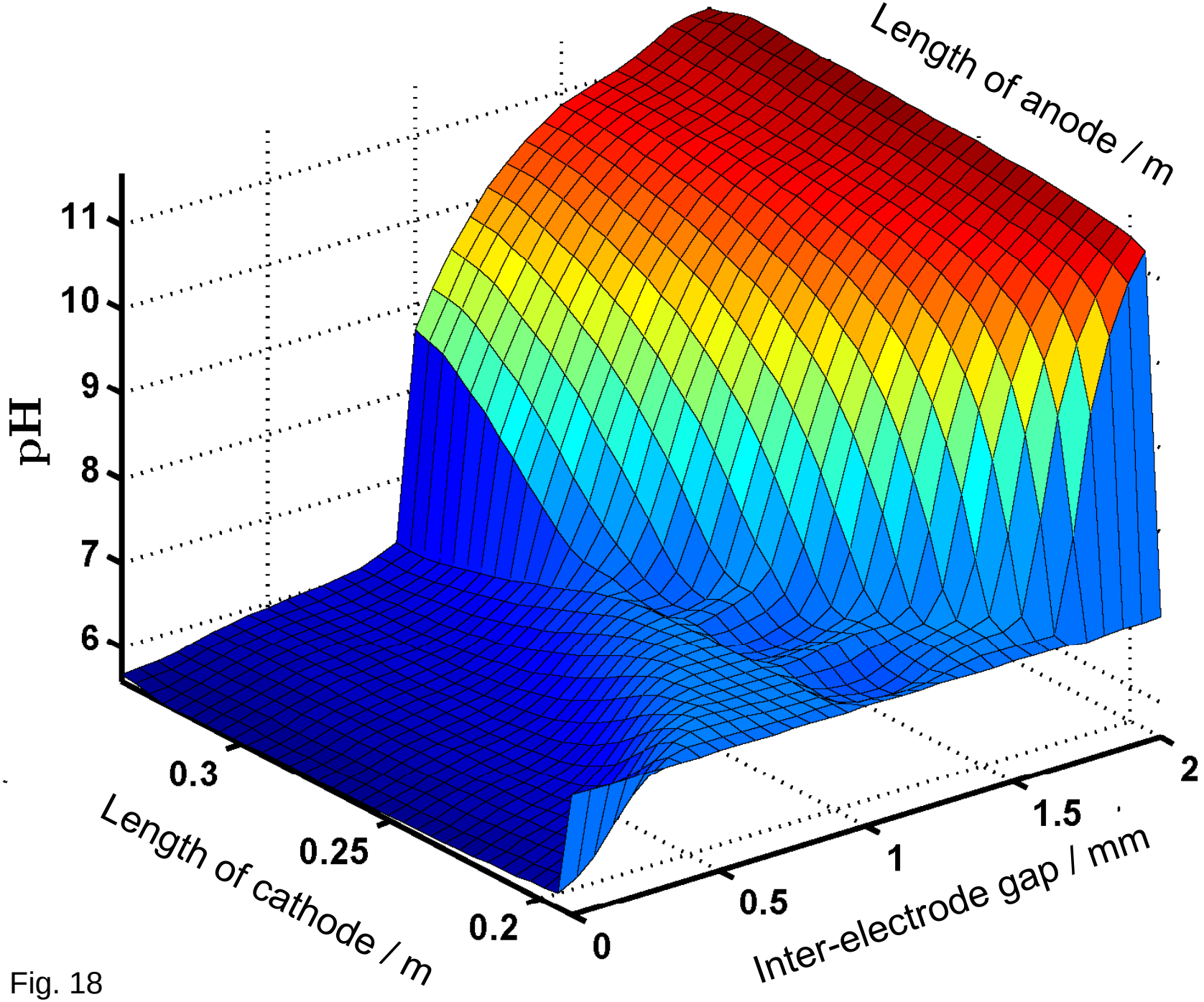

Fig. 18

Table 1

Click here to download Table: Table 1.pdf

Impurity	Cu	Si	Fe	Mn	Mg	Zn
Content limit / wt. %	0.05	0.25	0.4	0.5	0.05	0.05

Table 1

Table 2
Click here to download Table: Table 2.pdf

electrode type	pure Al ‘rough’	pure Al ‘smooth’	Al1050 ‘rough’	Al1050 ‘smooth’
purity	99.99%	99.99%	99.5%	99.5%
roughness R_a / μm	1.340	0.062	1.041	0.088
electrode area / m^2	3.9×10^{-5}	2.1×10^{-5}	3.72×10^{-5}	4.22×10^{-5}
current density / A m^{-2}	2.56	4.76	2.69	2.37

Table 2

Table 3

Click here to download Table: Table 3.pdf

solution		*0.5 mol m^{-3} sulphate*		
electrode potential / V(SCE)		-1,0	-0,6	-0,2
R_e / ohm m^2		1,17E+03	1,75E+03	2,78E+03
R_1 / ohm m^2		2,34E+03	2,62E+03	2,30E+03
R_2 / ohm m^2		3,25E+04	7,49E+04	1,16E+05
CPE_1	***Y_0 / ohm s^n***	3,31E-06	1,53E-06	1,02E-06
	n	0,956	0,966	0,970
CPE_2	***Y_0 / ohm s^n***	1,10E-05	2,39E-06	2,17E-06
	n	0,428	0,571	0,662
ω_{max} for CPE_1 / Hz		1,39	1,00	0,52

Table 3